IFSA

Sergey Y. Yurish
Editor

Advances in Signal Processing

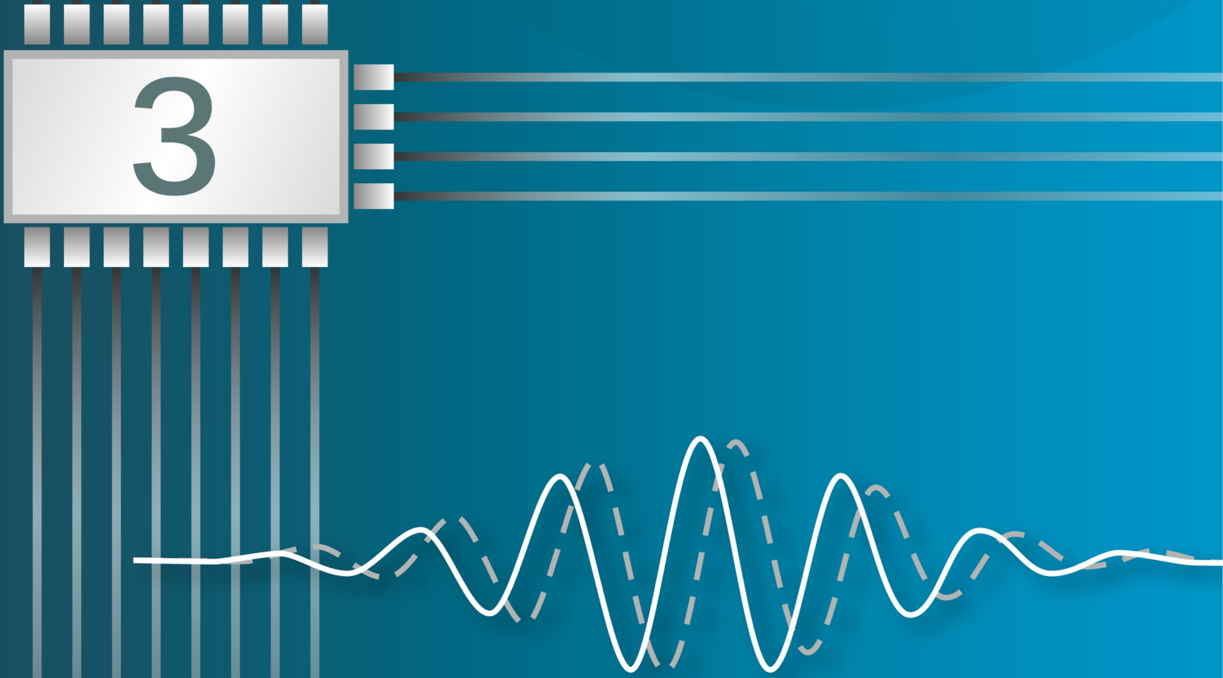

Advances in Signal Processing

Book Series, Volume 3

Sergey Y. Yurish
Editor

Advances in Signal Processing

Book Series, Volume 3

International Frequency Sensor Association Publishing

Sergey Y. Yurish
Editor

Advances in Signal Processing
Book Series, Volume 3

Published by International Frequency Sensor Association (IFSA) Publishing, S. L., 2025
E-mail (for print book orders and customer service enquires): ifsa.books@sensorsportal.com

Visit our Home Page on http://www.sensorsportal.com

ISBN: 978-84-09-69173-9
BN-20250419-XX
BIC: UYS

Acknowledgments

As Editor I would like to express my undying gratitude to all authors, editorial staff, reviewers and others who actively participated in this book. We want also to express our gratitude to all their families, friends and colleagues for their help and understanding.

Contents

Contributors .... **IX**
Preface .... **XI**

1. Wearable PPG Sensors Applicable for Measurement in a Weak Magnetic Field Environment of an MRI Device **1**

1.1. Introduction 1
1.2. A PPG Sensor: Principle, Structure, and Function 3
1.2.1. Basic Description of Wearable PPG Sensors *3*
1.2.2. Description of Realized Wearable PPG Sensors *6*
1.2.3. Description of the Control Application Based on Windows Platform *9*

1.3. PPG Signal Properties, Processing, and Analysis 12
1.3.1. Basic Description of PPG Signal Properties and Processing *12*
1.3.2. Determination of PPG Wave Parameters *13*

1.4. Evaluation of Precision of Realized PPG Sensors 17
1.5. Conclusions and Future Work 19
Acknowledgements 20
References 20

2. Linearization and Integerization for Computing Algebraic Matroids **23**

2.1. Introduction and Motivation 23
2.2. Background 25
2.3. Algorithmic Approaches to Algebraic Matroids 26
2.4. Results and Conclusions 34
2.5. Future Work 36
References 36

3. Holotomography Approach for the Detection and Segmentation of Amoebas in Water Samples Using Active Contour **39**

3.1. Introduction 39
3.2. Materials and Methods 41
3.2.1. Experimental Setup *41*
3.2.2. Detection Phase *41*

3.3. Results and Discussion 46
3.3.1. Detection Evaluation *46*
3.3.2. Segmentation Evaluation *47*

3.4. Conclusion 49
Acknowledgment 49
References 49

Contributors

David Ash
Real Time Agents Inc, 191 Twinbridge Cir, Pleasant Hill, CA 94523, USA

Abdenbi Bouzid
Hassan I University, Faculty of Science and Technology, Higher Institute of Health Sciences, Settat, Morocco

Anass Cherkaoui
Hassan I University, Faculty of Science and Technology, Higher Institute of Health Sciences, Settat, Morocco

Abdelaziz Essadike
Hassan I University, Faculty of Science and Technology, Higher Institute of Health Sciences, Settat, Morocco

Ivan Frollo
Institute of Measurement Science, Slovak Academy of Sciences, Bratislava, Slovakia

Jiří Přibil
Institute of Measurement Science, Slovak Academy of Sciences, Bratislava, Slovakia

Anna Přibilová
Institute of Measurement Science, Slovak Academy of Sciences, Bratislava, Slovakia

Preface

It is a pleasure to present Volume 3 of the book series *Advances in Signal Processing*. This volume continues the series' mission to showcase high-quality contributions that reflect both the theoretical foundations and the rapidly expanding application landscape of modern signal processing. Across its chapters, the reader will find a balanced blend of wearable sensing and biomedical signal acquisition, mathematical and algorithmic methods with relevance to data and signal models, and computational imaging for detection and segmentation tasks—three directions that increasingly converge in today's interdisciplinary research and development.

Chapter 1 addresses a practical and demanding measurement scenario: capturing physiological signals reliably in the environment of an MRI system. The chapter discusses the realization of special-purpose wearable photoplethysmography (PPG) sensor prototypes and the supporting hardware/software design choices needed for operation in a weak magnetic field and shielded surroundings. Particular emphasis is placed on sensor architecture, wireless communication strategies, sampling and storage modes, and processing steps for extracting heart-rate–related information from PPG waveforms. By connecting engineering constraints (electromagnetic compatibility, shielding, materials) with signal acquisition and analysis requirements, this chapter offers a valuable reference for researchers and practitioners working on biomedical instrumentation, wearable monitoring, medical imaging environments, and robust physiological signal processing.

Chapter 2 moves to the methodological core of modern computational mathematics with direct implications for modeling and inference problems. Algebraic matroids provide a framework for understanding dependency structures among variables—an issue that appears in many signal processing and data-driven applications, including system identification, model discrimination, compressed sensing, and structured reconstruction problems. The chapter motivates why scalable computation of algebraic matroids matters, outlines background concepts (independence, bases, circuits), and explores algorithmic strategies such as linearization and integerization alongside classical symbolic approaches. Readers will gain insights into how dependency information can be extracted without committing to specific parameter values, which is particularly useful when systems are complex, partially observable, or prone to uncertainty. This chapter will be especially useful for those interested in applied algebra, computational methods, model-based data analysis, and advanced signal processing theory.

Chapter 3 demonstrates the role of signal processing in computational imaging and environmental/biological monitoring. Using holotomography-based imaging as a starting point, the chapter presents a workflow for detecting and segmenting amoebas in water samples, with active contour techniques supporting accurate boundary extraction. The emphasis on detection evaluation and segmentation performance connects algorithm design with measurable outcomes—an increasingly important requirement for real-world deployments. This contribution will interest readers working in image and video processing, biomedical and microscopic imaging, pattern recognition, and automated inspection systems, especially where reliable segmentation is a critical step.

Taken together, the three chapters illustrate how signal processing now spans hardware-aware acquisition, mathematical structures for inference and identifiability, and data-driven imaging pipelines. Accordingly, this volume should prove useful to a broad audience: graduate students seeking well-motivated examples and methods; academic researchers exploring cross-disciplinary directions; and engineers developing practical systems in healthcare, sensing, imaging, and analytics. We hope that the ideas collected here will not only inform current work but also inspire new collaborations across the diverse communities that contribute to—and benefit from—advances in signal processing.

Dr. Sergey Y. Yurish

Editor
IFSA Publishing *Barcelona, Spain*

Chapter 1

Wearable PPG Sensors Applicable for Measurement in a Weak Magnetic Field Environment of an MRI Device

Jiří Přibil, Anna Přibilová and Ivan Frollo

1.1. Introduction

Magnetic resonance imaging (MRI) devices are widely used in modern clinical practice for non-invasive imaging of different parts of a human body. The MRI method can be useful also for creation of 3D human vocal tract models to examine dynamic changes in the shape of the vocal folds [1]. Next, the MRI tomography is suitable in the area of medical diagnostics – for classification and detection of Alzheimer's disease and other neurodegenerative disorders [2, 3]. The MRI tomographs are also often applied for monitoring of therapy progress after vocal fold cancer surgery, for evaluation of human knee cartilage [4], etc.

From the construction point of view, there exist two types of MRI scanners – the open-air ones used mainly for scanning of peripheral parts of the human body (arm, leg, knee, etc.) and the whole-body ones for widespread usage in MR imaging. MRI devices also differ in the working magnetic field used: open-air types usually work with a weak field (up to 0.2 T) [5], the whole-body types work with stronger basic magnetic fields (at present up to 11 T) [6]. Every MRI device consists of a gradient system to select x, y, and z slices of a tested object/subject situated inside the scanning area together with a radio frequency (RF) receiving/transmitting coil for generation of excitation pulses and catching an answer in the form of a free induction decay (FID) signal [7, 8]. In the open-air MRI system, planar gradient coils [9] are mostly used to minimize space requirements. The closed-bore (also called whole-body) MRI devices typically use cylindrical gradient coils distributed around the tube in which an examined person/object lies [10]. In both types of MRI equipment, rapid switching of large currents flowing through metal conductors of the gradient coils generates significant mechanical vibration and loud acoustic noises [8].

Jiří Přibil
Institute of Measurement Science, Slovak Academy of Sciences, Bratislava, Slovakia

Their intensity depends on the used type of a scan sequence and its parameters – sequence type, repetition time, echo time, slice orientation, etc. [7] as well as the volume inserted in the scanning area of the MRI device [11].

Due to electromagnetic compatibility and reduction of possible RF signal interference, the whole-body MRI scanning equipment is typically located inside a solid metal cage (often made from Cu plates). In the case of the open-air low field MRI device, this cage is made from a steel plate with thickness of about 2 mm with symmetrically placed small holes to eliminate electromagnetic field propagation to the surrounding space (a control room with an operator console, etc.) [9]. Therefore, using direct cable connection between sensors (measuring instruments) and evaluation/control unit (devices) located outside the shielding cage is practically very difficult to realize. On the other hand, the mentioned small holes in the steel plates practically enable wireless communication (via Wi-Fi or Bluetooth – BT) between the active scanning area and the control room with an operation console of the open-air MRI equipment. Investigations performed previously confirm the possibility of the data transfer through the closed door of the shielding metal cage [12], [13]. Therefore, the wireless communication based on BT connection is practically realizable and wearable sensors accessed by a bi-directional BT module are fully usable for this task. In addition, the performed analysis confirms that the BT communication inside the shielding cage does not interfere with the signals of RF coils and has no visible effect on the final quality of MR images [13]. On the other hand, the wearable sensors placed in the MRI scanner must not contain any metal part from ferromagnetic materials, to eliminate any interaction with a working magnetic field. It is important for preserving maximum quality of MR images without any artifacts. Due to strong RF disturbance, all parts of the sensor must be shielded by aluminium or brass boxes to prevent a damage of internal electronic circuits [13].

The general disadvantage of the MR scanning process consists in a fact that examined persons lying inside the running MRI scanner are exposed by noise and vibration causing them stress and other physiological or psychological negative effects. The level and impact on the scanned person depend on applied exposition time and intensity of vibration and acoustic noise. Negative impact to an examined person is manifested mainly by heart rate (HR) and arterial blood pressure (ABP) changes [14], which can be monitored during the MR scanning process. The HR values and their changes can be detected and evaluated from the signal sensed by an optical sensor working on a photoplethysmography (PPG) principle, while the systolic or diastolic blood pressure values are usually measured by a blood pressure monitor device (BPM) [15]. The PPG measurement uses an optical sensor for non-invasive pickup of vital functions of the vascular system from the skin [16] by detecting blood volume changes inside the tissue. Obtained PPG signals can be next used to determine other specific parameters applicable in systems for medical assessment [17], and/or utilized for biometric authentication [18]. At present, several cuffless techniques based on estimation of ABP values directly from one or more-channel PPG waves sensed simultaneously [19] are often applied. These methods use several time domain parameters, energetic, and spectral features determined from the recorded PPG waveform(s). The ABP values may be assessed with higher precision when are used – typical representatives of these parameters are the pulse transmission time (PTT) and the pulse wave velocity

(PWV) [20]. If PTT is used in addition to PPG, the estimated BP values are more accurate [21, 22] because of linear relation between the PTT and ABP values [23, 24].

This chapter describes realization, testing and practical experiments with developed special prototypes of wearable PPG sensors applicable for real-time sensing of one, two, and/or thee-channel PPG waves with wireless data transfer to a control device – all in the environment of the open-air low field MRI tomograph. Basic working principles and realizations of the optical part of the PPG sensor are also discussed here. The chapter continues with description of structures and basic functional parts of the developed wearable sensors. Next, the communication and control strategy used for real-time data transfer and PPG samples storage in a control device is discussed. Then the chapter follows a detailed description of created control application for Windows platform – all operating elements on the control panel are explained here. Description of the method used for determination of different parameters from the sensed PPG wave(s) with respect to unipolar representation of the PPG signal(s) is presented next. Last but not least, the comparative measurements performed with the certified commercial pulse oximeter (OXI) device and the clinical BPM device for evaluation of stability and precision of the determined HR values was mentioned in this study.

1.2. A PPG Sensor: Principle, Structure, and Function

1.2.1. Basic Description of Wearable PPG Sensors

In general, an optical sensor working on a photoplethysmography principle can operate in a transmittance or a reflectance mode [25]. The transmittance type of a sensor probe has usually a form of a finger ring or an ear clip with a light source (one or more LED elements) and a photo detector (PD) placed on opposite sides of the sensed human tissue – see a principal example in Fig. 1.1a). For the reflectance sensor type holds that the PD element measures the intensity of the light reflected from the skin and it is placed on the same side of the skin surface as the light source transmitter – see principal examples in Fig. 1.1b). This type an optical sensor is placed mainly on fingers or a wrist, typically fixed by an elastic/textile ribbon or it is integrated as a part of different wearable devices – fitness bracelets, smart watches, etc. In both cases, the signal from PD that is next amplified and filtered represents a dynamic component – DC part of the photoplethysmography signal [26]. The PPG signal consists of typical systolic and diastolic peaks (an example in Fig. 1.1c). The systolic peak on the PPG wave directly corresponds with a heart activity – it is derived from the *R* peak of the electrocardiogram (ECG).

The wearable PPG sensor enabling the real-time, continual PPG signal measurement consists principally of four basic functional parts:

- A microcontroller or DSP processor board with integrated A/D convertors, including also a hardware SPI/I2C port, and an UART to USB interface;

- A BT receiver/transmitter for serial bi-directional communication with control device(s);
- One or more optical pulse PPG sensors working in a reflectance or transmittance mode with fully integrated analogue interfaces;
- A power supply part as shown in a principal diagram of a three-channel PPG sensor structure presented in Fig. 1.2.

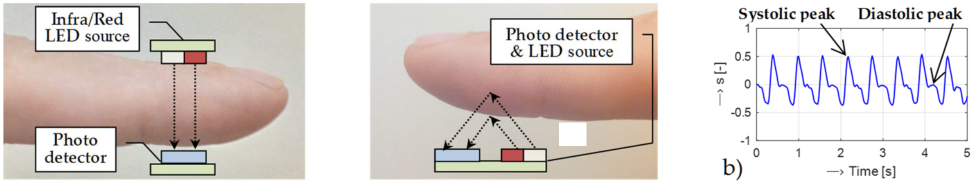

a) b) c)

Fig. 1.1. Basic principle of PPG sensors working in: a) Transmittance; b) Reflectance modes; c) Example of sensed PPG wave.

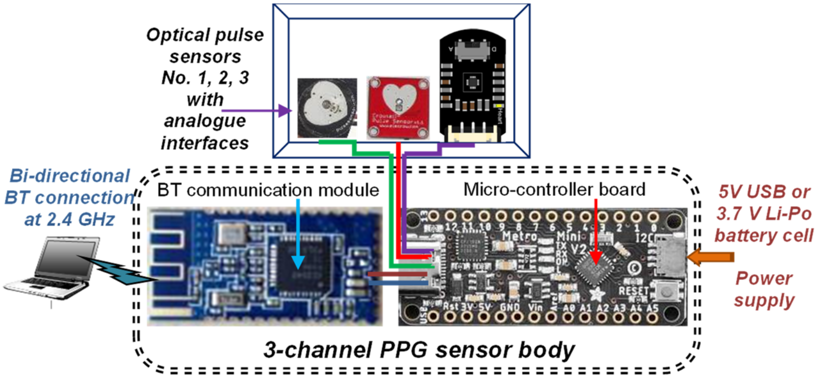

Fig. 1.2. Principal structure diagram of a wearable three-channel PPG sensor.

The power supplying the whole sensor can be realized using the rechargeable polymer-lithium-ion (Li-Po) cells with output voltage of 3.7 V, or by 5 V external power banks via the USB port independence of used micro-controller board (using 3.3 V or 5 V logic levels). The BT modules as well as the optical pulse sensors usually can work with both voltage levels without any additional signal conversion requirements. The capacity of the power supply device used finally depends first of all on the resulting DC current of the whole sensor, the required time duration for continual measurement, the maximum sampling frequency f_S for sensing of PPG signal(s), and the maximum serial communication rate for real-time data transfer to the control device. Processors working at the voltage level of 3.3 V have typically the clock frequency of 8 MHz, so the maximum f_S = 500 Hz and communication at the baud rate of 57600 bps could be achieved. In this case, using of Li-Po batteries with capacity from 125 to 750 mAh is proper for normal experimental purpose. Microcontrollers and processors operating at the 5 V voltage level work usually with f_{CLK} = 16 MHz, so higher sampling frequency up to 1 kHz and higher serial communication rate of 115200 bps could be reached. On the other hand, this type of PPG sensor has also higher requirements on the capacity of the powering part. For long-time experiments the power banks with capacity from 2000 to 5000 mAh are suitable to guarantee safety and stable supplying for the whole-time duration of the measurement.

A relatively high sampling frequency of at least 500 Hz is necessary to perform the analysis of morphological features of the individual PPG pulse waves [27] as well as to determine PTT and PWV parameters with high precision. On the other hand, commercially available PPG devices typically sample the PPG signal at low frequencies (from 50 to 100 Hz) [25]. Lower sampling frequencies are also suitable for continual long-term acquisition of the PPG signal, e.g., sampling at 128 Hz was used by [17] for atrial fibrillation monitoring with the PPG sensor on a wrist.

The whole sensor can work in “Slave” or “Master” mode depending on the sensing and data transmission strategy used. We are oriented to the control strategy when the PPG sensor works as a “slave”, i.e. after initialization it waits for commands from the master external device (notebook, desktop PC, etc.) via the BT communication. The service program on a microcontroller board enables adjustment of the time delay T_{INT} (internal interrupt clock) to read the analog signal and make A/D conversion. It means analogue signals from the optical PPG parts are sensed at the sampling frequency f_{S} corresponding to the chosen T_{INT} value. Next, the data block size N_{MEAS} of 16-bit PPG signal samples are set for transmission to the control device. Finally, the number of used channels – number of optical pulse sensors to be read – must be adjusted and size of head communication data buffers must be set. On the side of a control device, the application must control acquisition of one or more-channel PPG signals, their processing, and data storage. This application was mostly created for Windows platform working on standard PC desktop or portable laptop devices. It is also possible to create an application under Android platform for implementation on mobile devices (tablets and/or smartphones). Practically, the control application performs two basic tasks:

1. Real-time monitoring and displaying of PPG signals picked up currently from one or more optical PPG sensors;
2. Continuous PPG signal measurement with the selected sampling frequency f_{S} in data blocks of N_{MEAS} samples.

Within the real-time PPG signal(s) measurement following operations can be also performed:

- direct storing the received samples of the PPG signal to a file on the disk of the master device without any next processing using the commands “Start” and “Stop” sent manually by the user;
- storing the PPG signal samples to an internal memory buffer enabling to perform post-processing operations as filtering and HR determination; in this way the modified data can be stored off-line to the file(s) by the application user.

Operating in the measurement mode denotes that the data block with chosen dimension and structure of PPG signal samples from one or more optical pulse sensor(s) are automatically transmitted to a control device in the frame of real-time operation. The sensed PPG signal(s) are subsequently stored in a Wave format (with 16-bit quantization, mono, PCM coding). These PPG wave records can be further processed and analyzed off-line, for example in the Matlab program environment.

1.2.2. Description of Realized Wearable PPG Sensors

In the frame of our long-term research aim to apply PPG sensors in the measurement inside the scanning low-field MRI tomograph, several special prototypes were developed. The main motivation was to realize wearable PPG sensors representing a low-cost solution, but fully operational for our experimental purpose. Five prototypes of PPG sensors were subsequently realized within last five years – three one-channel prototypes, one consisting of three optical pulse sensor parts, and one prototype enabling sensing of a two-channel PPG signal in parallel (further called as “PPG-EP”, “PPG-PS1”, “PPG-BLE”, “PPG-2Tp”, and “PPG-3p” – see details in Table 1). They next differ in the type of optical parts (of the reflectance/transmittance design), type of BT communication module, and used voltage level for power supply.

To eliminate the mentioned interaction with the magnetic field and prevent possible disturbance in electromagnetic compatibility inside the running MRI equipment, the processor board with the BT module as well as the optical sensor are covered in two separate aluminium shielding boxes as documented by the photos in Fig. 1.3.

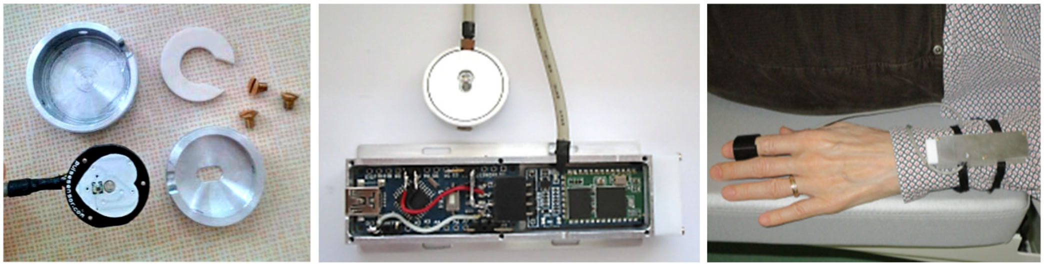

a) b) c)

Fig. 1.3. Example of assembling and covering of: a) Optical Pulse sensor; b) Micro-controller board with BT communication module (sensor’s body) with closed optical sensor part; c) Closed body and optical part of the PPG sensor worn on a left hand without power supplying [13].

On the side of the micro-controller part, all sensors have been realized with the help of the open-source development platform Arduino boards [28]) based on the 8-bit processor ATmega328 by Atmel company with integrated eight 10-bit A/D converters. It means that the sensed PPG signal has the theoretical maximum value given by the number of bits of the A/D convertor and practically denoted by the used voltage level (5/3.3 V) of the power supply. Following types of Arduino compatible boards were stepwise used:

1. Arduino Uno ver. 3.0 board [29] or Nano ver. 3.0 board [30] based on the Atmel processor ATmega328P with $f_{\mathrm{CLK}} = 16$ MHz (operating at 5 V level) with an integrated USB interface for serial programming and testing;

2. Arduino Pro Mini v. 2.0 board [31] also with the processor ATmega328 but without the USB interface and running at $f_{\mathrm{CLK}} = 8$ MHz and operating at 3.3 V level;

3. Adafruit Metro Mini 328 board (Arduino compatible) based on the processor ATmega328P, including also hardware SPI and I2C ports, and an UART to USB interface [32].

For wireless communication between the control device and the PPG sensor, two types of BT modules working at 2.4 GHz were used:

- BT communication module HC-06 (Waveshare 4328 [33]) fully compatible with the Arduino platform, working in BT 2.0 standard with the maximum baud rate of 115200 bps;

- BT module MLT-BT05 by Techonics, Ltd. [34], working in BT4.1 BLE (low energy) standard, supporting also the serial baud rate up to 115200 bps.

The PPG also sensors differ in the used optical pulse sensor parts. Following three types of optical sensors with fully integrated analogue interfaces were applied in the developed PPG sensors:

- the Pulse Sensor Amped (Adafruit 1093) by Adafruit Industries [35];

- the Crowtail-Pulse Sensor (ER-CT010712P) by Elecrow Company [36];

- the Gravity Heart Rate Sensor (SEN0203) by Zhiwei Robotics Corp. [37].

Due to a reflectance principle, the sensor's photo detector and light source elements are placed on the same side of the skin surface on fingers or a wrist fixed by an elastic/textile ribbon. Next, two types of sensors working on the transmittance principle were applied in the PPG sensor prototypes:

- the Easy Pulse sensor v 1.1 analogue module (ER-CDE10301E) by Embedded Lab, with the optical sensor HRM-2511E by Kyoto Electronic Company [38],

- the Easy Pulse Mikro – a micro Bus compatible pulse sensor (designed by Embedded Lab) including the PPG optical pulse sensor ER-CDE17527M by Kyoto Electronic Company [39].

While the reflectance sensors have fully integrated analogue interface on the main board together with LED source and photo detector elements (see photos of Adafruit 1093, ER-CT010712P, and SEN0203 sensors in Fig. 1.4a-c), the transmittance types have an analogue interface located on a separate board and an optical part practically realized in the form of a rubber finger ring – see an example of HW realization in Fig. 1.4d-e.

With respect to expected long-term measurement experiments or for using multi-channel PPG sensor realizations, the whole sensor was powered via the USB port by the 5 V power bank THAZER (with 2200 mAh capacity), or by RealPower PB-4000 (4000 mAh). For short-time experiments using 3.3 V level devices, the 3.7 V textile battery (rechargeable Li-Po cell) with capacity of 125 mAh (for one-channel sensors) or with the capacity of 750 mAh (in the case of two-channels sensor) were applied, as documented by photos in Fig. 1.5. Differences in the architecture, the basic components used, the electrical and mechanical parameters of all developed PPG sensor prototypes are shown in Table 1.1.

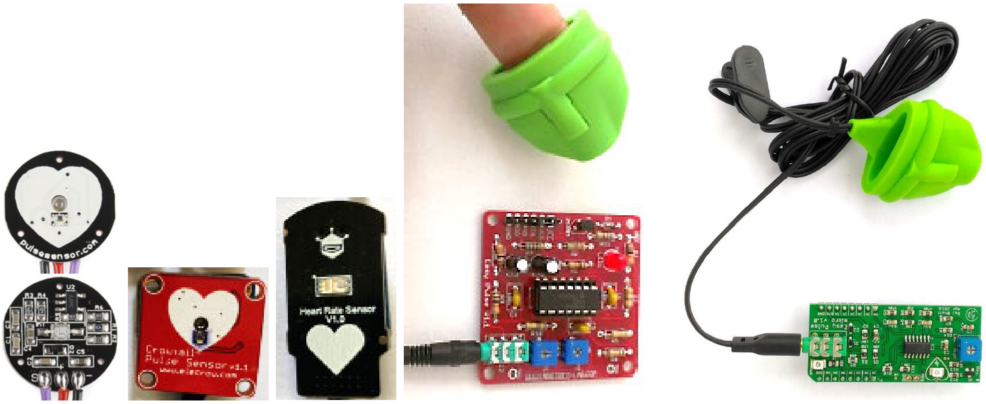

a) b) c) d) e)

Fig. 1.4. Example of HW realization of commercial heart pulse sensors: a) Front and back side of the Pulse Sensor Amped [35]; b) Front side of Crowtail-Pulse Sensor [36]; c) Front side of the Gravity Heart Rate Sensor [37]; d) Easy Pulse sensor v 1.1 analogue module [38]; e) Analogue board Easy Pulse Mikro connected with the ER-CDE17527M optical sensor [39].

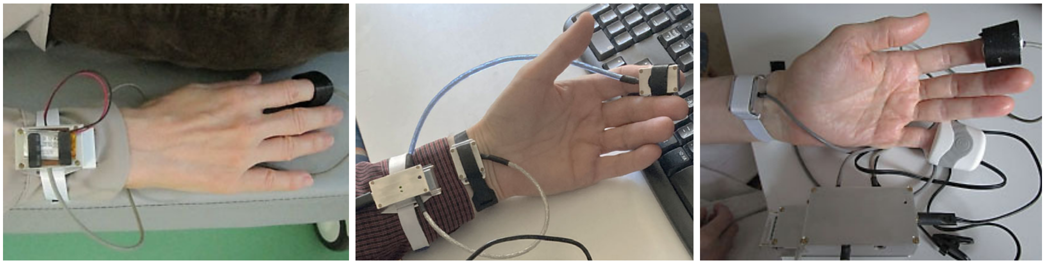

a) b) c)

Fig. 1.5. Example of realization, wearing and powering of developed PPG sensors: a) One-channel protype with mounted a 3.7 V Li-Po battery cell; b) Two-channel protype using two reflectance optical sensors; c) Three-channel protype consisting of one transmittance and two reflectance optical sensors; both multi-channels realizations are supplied by a 5 V power bank [13].

Table 1.1. Differences in architecture, basic components, mechanical and electrical parameters, for all five developed PPG sensor prototypes.

Params.	**Prototype name**				
	PPG-EP	**PPG-PS1**	**PPG-BLE**	**PPG-2Tp**	**PPG-3p**
No of channels	1	1	1	2	3
Optical sensor(s)	HRM-2511E	Adafruit 1093	Adafruit 1093	ER-CT010712P + SEN0203	2x Adafruit 1093 + ER-CDE17527M
Working mode	Trans.	Reflect.	Reflect.	2x reflect.	2x reflect. + 1x trans.
Arduino board	Uno v.3.0	Nano v.3.0	Pro Mini v. 2.0	Metro Mini 328	Nano v.3.3
BT module	HC-06	HC-06	MLT-BT05	MLT-BT05	HC-06
Voltage level	5 V	5 V	3.3 V	3.3/5 V	5 V
Mean DC current	60	26	14	20/31	38
Procs. f_{CLK}	16 MHz	16 MHz	8 MHz	8/16 MHz	16 MHz
Body dimensions (L×W×H)	105×70×80 mm	80×20×10 mm	40×25×15 mm	46×25×12 mm	80×33×30 mm
Body weight	445 g	55 g	40 g $^{1)}$	45 g $^{1)}$	180 g $^{2)}$

$^{1)}$ without mounted a Li-Po battery cell

$^{2)}$ together with the analogue board EasyPulse Mikro

1.2.3. Description of the Control Application Based on Windows Platform

Originally, each of the PPG sensors developed sequentially had an own Windows application for a control device. At present, one universal application called *PPGsensUniv.exe* was built. It enables control of one, two, or three-channel PPG signal acquisition, post-processing operation and PPG records storage for all of five realized PPG sensor prototypes, and communication with different types of PPG sensors in three functional modes:

1. Off-line, i.e., without any BT communication – only stored PPG waves can be shown, analyzed, and processed;
2. Automatic, i.e., with automatic connection to a pre-defined type of a PPG sensor (by initial setting of program parameters stored in *.INI files for each of sensor types) – real-time PPG signal monitoring and/or continual measurement in data blocks (including subsequent storing of received data to an external file);
3. Manual, beginning with the application start without BT connection, proceeding with a manually established connection to a chosen type of a PPG sensor and communication parameters (serial channel type, baud rate, BT 2.0 / BT 4.1 BLE protocol, etc.) working in a similar way as in the automatic mode.

Within the manual function it is also possible to manually disconnect the currently chosen PPG sensors and/or create a connection with another PPG sensor using different parameters. Due to the real-time requirement, only the following settings are possible: T_{INT} = {10, 8, 5, 4, 2, and 1 ms} representing the sampling frequencies f_{S} = {100, 125, 250, 500, and 1000 Hz} in the data blocks of N_{MEAS} = {1k, 4k, 16k, 32k, and 64k} of 16-bit samples after A/D conversion.

An example of a screen copy of the main control window of the application *PPGsensUniv* (version 1.03, actually connected with the three-channel PPG sensor PPG-3p) is shown in Fig. 1.6. The main window can be divided into seven areas "A"-"G" in correspondence with different control functions and operations:

1. Area "A" – place for displaying the sensed PPG signals together with their selected signal thresholds for systolic peak detection and HR determination operations (see a green dashed line); the threshold can be set automatically or manually by a slider tool located on the right of the graphics area. Next, we can see the displayed sequence of HR values determined per a heart pulse period from the selected PPG channel (drawn at bottom, by a green solid line). This display area is also used as a graphical output for function during the monitoring operation. In this case, the HR sequence is shown after stopping this process (from the last 1k-sample data block).
2. Area "B" – field of PPG channel parameters enabling: inversion operation (buttons *Inv*), signal amplification (buttons *G*), and absolute offset shift (buttons *O*) for each of the channels separately.
3. Area "C" – upper part consisting of switches to select the active PPG channel for HR determination and panel with the mean HR value for the whole PPG record; lower part with switches for PPG signal filtering and automatic threshold calibration.
4. Area "D" – set of buttons for managing and manual controls of graphical output (zoom in/out, redraw, clear and initialize the drawing area).
5. Area "E" – part for saving of the currently selected PPG signal(s) to an output file (in binary or ASCII format) or loading a previously stored file with PPG signals. In the right part, there are also placed panels with information about parameters of the currently sensed or loaded PPG signals: number of channels, length of data in samples, used sampling frequency.
6. Area "F" – the main part for managing and control of PPG signal monitoring, real-time receiving of PPG signal samples to an internal memory, or direct storing to an output file. Next, this area consists of buttons for starting/finishing (*Monit*/*End*) the monitoring operation and one button (*Read*) for manual start of the automatic PPG signal pickup. There are also info panels about the chosen number of samples to be sensed (N_{MEAS}), the time interrupt T_{INT} in ms to take a PPG signal sample(s) together with automatically adjusting of f_{S} in Hz), and the pre-calculated time duration value in seconds for the actual sensing operation.
7. Area "G" – the system setting and info part showing current status of connection with a chosen type of PPG sensor (name of sensor, associated serial communication channel and data transfer rate), pop-up selector for choice of PPG sensor, button for calling of a dialog window to set other system parameters, and finally the exit button for closing

the whole application (after closing all BT connections and open graphical/dialog windows).

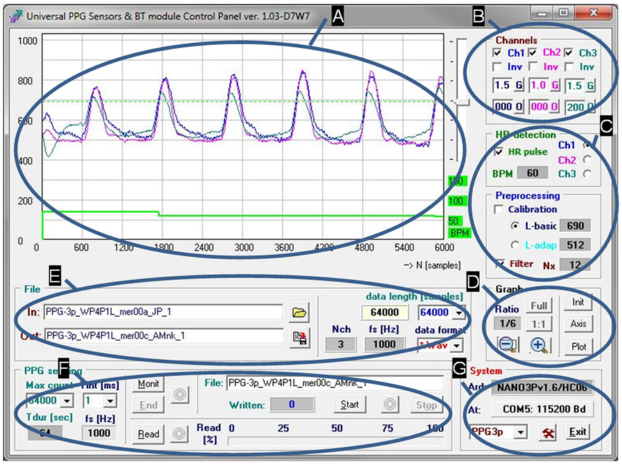
Universal PPG Sensors & BT module Control Panel ver. 1.03-D7W7

Channels: ☑ Ch1 ☑ Ch2 ☑ Ch3; ☐ Inv ☐ Inv ☐ Inv; 1.5 G, 1.0 G, 1.5 G; 000 0, 000 0, 200 0

HR detection: ☑ HR pulse; BPM 60

Preprocessing: ☐ Calibration; ● L-basic 690; ○ L-adap 512; ☑ Filter Nx 12

In: PPG-3p_WP4P1L_mer00a_JP_1

Out: PPG-3p_WP4P1L_mer00c_AMnk_1

data length [samples]: 64000, 64000

Nch: 3; fs [Hz]: 1000; data format: *.wav

Graph: Ratio 1/6

PPG setting: Max count 64000; Tint [ms] 1; Tdur [sec] 64; fs [Hz] 1000

File: PPG-3p_WP4P1L_mer00c_AMnk_1

Written: 0

System: Ard: NANO3Pv1.6/HC06; At: COM5: 115200 Bd; PPG3p

Fig. 1.6. Screen copy of the control application *PPGsensUniv* – actually selected function with a three-channel sensor *PPG-3p*.

The activated parameter setting window with shown listing during establishing of the BT connection with the PPG sensor working at the standard 4.1 BLE – transmitted and received AT commands for MLT-BT05 module can be seen in Fig. 1.7a. A simple communication during connection creation using the BT 2.0 standard for HC-06 BT module is shown in Fig. 1.7b. This window of communication parameters also enables setting of an actual serial channel (associated with a paired BT device), a current serial rate in bauds, a time duration for waiting response from the slave device, and the data format for commands and data transfer (text in ASCII or binary in 16-bit words). For the correct functionality with a chosen number of a serial channel, the BT pairing process must be performed first in the Windows control panel setting (outside of this application) – see an example in Fig. 1.8.

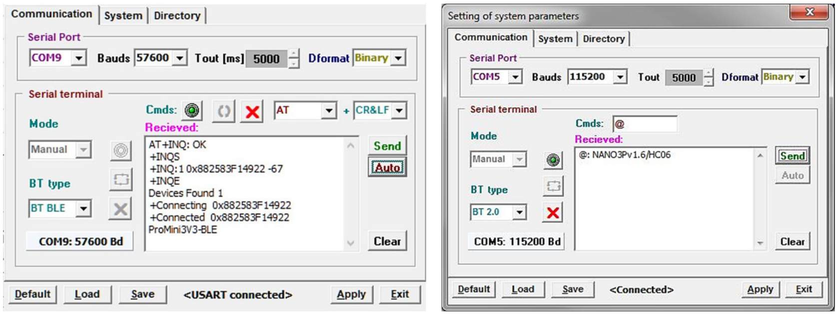
a) Serial Port: COM9; Bauds 57600; Tout [ms] 5000; Dformat Binary

Serial terminal: Mode Manual; BT type BT BLE; COM9: 57600 Bd; Cmds: AT + CR&LF

Recieved:

```
AT+INQ: OK
 +INQS
 +INQ:1 0x882583F14922 -67
 +INQE
Devices Found 1
 +Connecting  0x882583F14922
 +Connected  0x882583F14922
ProMini3V3-BLE
```

<USART connected>

b) Setting of system parameters

Serial Port: COM5; Bauds 115200; Tout 5000; Dformat Binary

Serial terminal: Mode Manual; BT type BT 2.0; COM5: 115200 Bd; Cmds: @

Recieved:

```
@: NANO3Pv1.6/HC06
```

<Connected>

a)　b)

Fig. 1.7. Screen copy of the dialog window for setting of system parameters currently displaying a section of BT connection and communication for: a) module MLT-BT05 with BT 4.1 BLE protocol [13]; b) module HC06 running at BT2.0 standard.

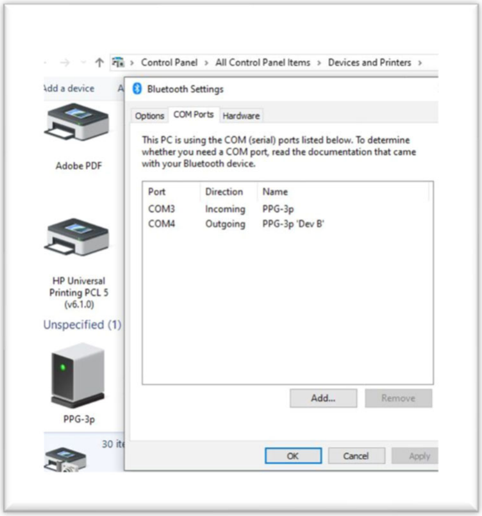

This PC is using the COM (serial) ports listed below. To determine whether you need a COM port, read the documentation that came with your Bluetooth device.

Port	Direction	Name
COM3	Incoming	PPG-3p
COM4	Outgoing	PPG-3p 'Dev B'

Fig. 1.8. Example of control panel in Windows 10 OS – the PPG3p sensor is associated with the system serial channel COM4.

1.3. PPG Signal Properties, Processing, and Analysis

1.3.1. Basic Description of PPG Signal Properties and Processing

From the physical principle follows that a great part of the PPG signal is composed of a direct current (DC) component corresponding to the whole blood volume of an examined tissue. The superimposed alternating current (AC) component follows the beating of the heart, so it carries also vital information including the heart rate. Its magnitude is much smaller (typically about 2-3 % of the DC component), as can be seen in a principal diagram in Fig. 1.9a.

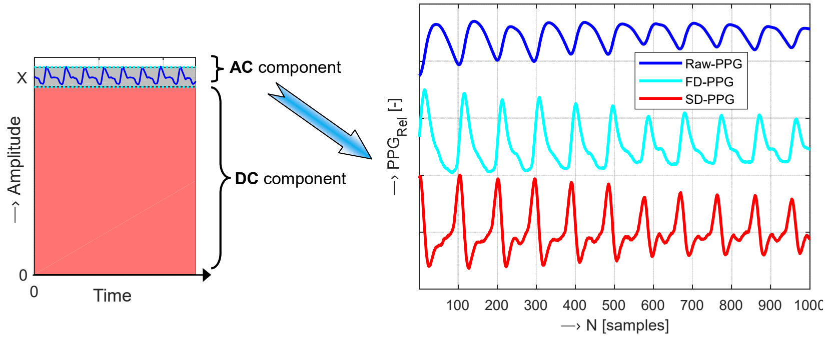

a) b)

Fig. 1.9. Principal structure of a PPG signal: a) Superposition of AC and DC components, b) 1k-sample example of PPG wave in three basic forms (raw PPG, FD-PPG, and SD-PPG).

A crucial step in the PPG pulse wave analysis is calculation of signal derivatives that may be used for determination of pulse wave features. The original pulse wave – (raw PPG), its first derivative (FD-PPG) – called also as velocity photoplethysmogram, and its second derivative (SD-PPG) – known as acceleration photoplethysmogram, are practically taken, processed, and analyzed [26]. The mentioned systolic and diastolic peaks are present in each cycle of the PPG wave (see the demonstration example of sensed PPG wave in Fig. 1.1c). They must be detected and localized for the purpose of further analysis. While the raw PPG signal is not suitable for local maxima determination, the FD-PPG and particularly the SD-PPG waves are more informative due to more pronounced local extrema as shows an example in Fig. 1.9b.

Generally, the picked-up PPG signal has an amplitude modulation with a partially linear trend (LT), it usually contains a superimposed noise component, and sometimes it is partially disturbed or degraded. Therefore, the sensed PPG signal must be pre-processed prior to further practical use. In the frame of the de-trending operation, the LT is calculated (usually by the mean square method) and applied within the LT removal procedure. Then, the PPG signal must be smoothed to eliminate local artifacts caused by signal noise or disturbance. In a lot of cases it seems to be sufficient to apply a moving average (MA) filter with the window length $w_{\mathrm{MA}} = 2N\mathrm{x}+1$. In this way we can obtain a clean PPG waveform describing actual condition of the cardiovascular system of a tested person. Three groups of PPG wave parameters are typically determined within the PPG signal analysis:

1. Temporal and energetic parameters: amplitude, signal range, and signal modulation;
2. Heart rate values and their statistical properties (variance, etc.);
3. Heart pulse transmission parameters - pulse transmission time (PTT) and pulse wave velocity (PWV).

1.3.2. Determination of PPG Wave Parameters

Most used algorithms work with a PPG wave in a relative bipolar presentation, such that the PPG signal lies in the range of ±1. As all the developed prototypes of PPG sensors produce absolute signals in the range of <0÷1024>, different approaches must be used or adopted in this situation. Because the analogue interface of optical sensors performs de-trending of the PPG signal during its cascade processing, this task cannot be solved in this case. Smoothing of sensed PPG signals is carried out by the MA filter with the N_{x} parameter chosen in dependence on the currently used sampling frequency. This operation is applied only once when the whole data block is transferred to the memory of the main control application. It means practically, that the PPG signal(s) continually displayed within the monitoring mode is not any filtered.

Analysis of the PPG signal pre-processed in this way starts with localization of systolic peaks P_{SYS} and heart pulse periods (T_{HP}). Our proposed method works in four steps:

1. Setting of the PPG signal threshold L_{THRESH};
2. Binary clipping of the input pulse wave;

3. Localization of the systolic peaks P_{SYS};
4. Determination of the heart pulse periods T_{HP}.

The level threshold can be set either manually individually for each of the processed PPG signals or adaptively – typically at one-third from the systolic pulse peak. During processing of the PPG signal with the length of P samples, the clipping operation produces a sequence $c_{PPG}(i)$ of values 1/0 corresponding to the input signal samples above/below the adjusted threshold level L_{THRESH} as

$$c_{PPG}(i) = \begin{cases} 1 & y(i) \geq L_{TRESH} \\ 0 & y(i) < L_{TRESH} \end{cases}, 1 \leq i \leq P \qquad (1.1)$$

The position of each of the systolic peaks P_{SYS} is basically determined as the middle of every T_1 interval. To localize P_{SYS} with higher accuracy it is necessary to pick up PPG signals with higher sampling frequency f_{S}. Therefore, the systolic peak position is finally set as the local maximum found in the T_1 interval – see an example in Fig. 1.10. The heart pulse periods T_{HP} are determined from this clipped sequence as the length of two adjacent continual parts of ones (with T_1 samples) and zeros (T_0 samples), i.e. $T_{\mathrm{HP}} = T_1 + T_0$.

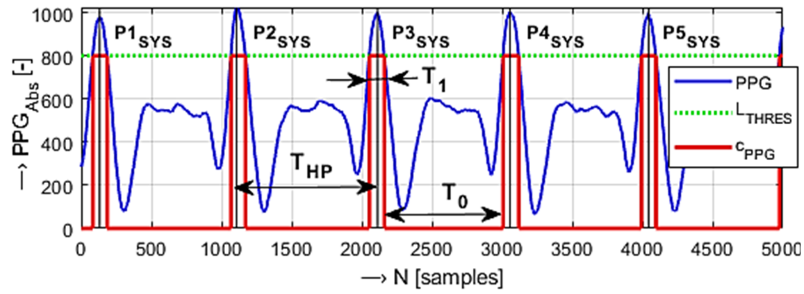

Fig. 1.10. An example of 5k-sample part of one-channel PPG signal together with: clipping sequence c_{PPG}, signed heart pulse period T_{HP}, and lengths of T_1, T_0 for the systolic pulse P3$_{\mathrm{SYS}}$; $L_{\mathrm{THRES}} = 800$.

Obtained systolic peak positions and lengths of heart pulse periods are subsequently used for determination of other PPG wave features. To obtain temporal and energetic parameters, the following operations and calculations are performed:

1. Finding of maximum and minimum levels of localized systolic peaks (Lsp_{MAX} and Lsp_{MIN}) together with the whole signal offset level (L_{OFS}). These levels are needed for calculation of the mean absolute systolic peak amplitude (SP_{AMPL}), using the mean signal offset value μL_{OFS} as

$$SP_{\mathrm{AMPL}} = (Lsp_{\mathrm{MAX}} + Lsp_{\mathrm{MIN}})/2 - \mu L_{\mathrm{OFS}}; \qquad (1.2)$$

2. Then, the relative systolic peak ripple SP_{RIPP} in percentage of a PPG wave (see demonstration example in Fig. 1.11) is calculated using the following formula

$$SP_{RIPP} = (Lsp_{\mathrm{MAX}} - Lsp_{\mathrm{MIN}}) / Lsp_{\mathrm{MAX}} \times 100; \quad (1.3)$$

3. Finally, the relative signal range (PPG_{RANGE}) in percentage can be determined from the absolute systolic peak amplitude SP_{AMPL} as

$$PPG_{\mathrm{RANGE}} = SP_{\mathrm{AMPL}} / AD_{\mathrm{NRES}} \times 100, \quad (1.4)$$

where the AD_{NRES} represents the numerical resolution of the currently used A/D converter. In our case, for all analyzed PPG signals the AD_{NRES} value was equal to 1024, since 10-bit A/Ds were used for digitalization of the analogue signal from the optical sensor ($2^{10} = 1024$).

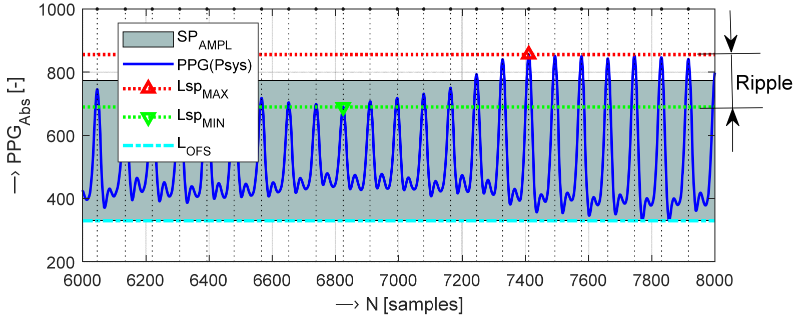

Fig. 1.11. An example of 2-k sample part of a PPG signal with localized systolic peaks P_{SYS} and their mean amplitude $\mathrm{SP_{AMPL}}$, determined Lsp_{MAX}, Lsp_{MIN}, and L_{OFS} levels used for ripple calculation.

Using the sampling frequency f_{S} in Hz and the heart pulse period T_{HP} in samples, the heart rate HR in min^{-1} can be easily calculated as

$$\mathrm{HR} = 60 \times f_{\mathrm{S}} / T_{\mathrm{HP}} \quad (1.5)$$

The heart pulse transmission parameters are determined from two PPG waves ($\mathrm{PPG_A}$, $\mathrm{PPG_B}$) sensed in parallel. It is important to localize precisely the systolic peak positions P_{SYS} in both PPG signals and to measure correctly differences between P_{SYS} in samples ($\Delta P_{\mathrm{SYSa,b}}$) – see a demonstration example for a two channel PPG signal in Fig. 1.12.

For the applied sampling frequency f_{S} expressed in Hz, the pulse transit time parameter (PTT in ms) is calculated as

$$PTT = \Delta P_{\mathrm{SYS}} / f_{\mathrm{S}} \quad (1.6)$$

When we know the distance between locations of the optical PPG sensors (Dx in m) and the pulse transit time parameter (PTT in s), then the pulse wave velocity parameter (PWV in m/s) [20] is calculated as follows

$$PWV = D\mathrm{x} / PTT \quad (1.7)$$

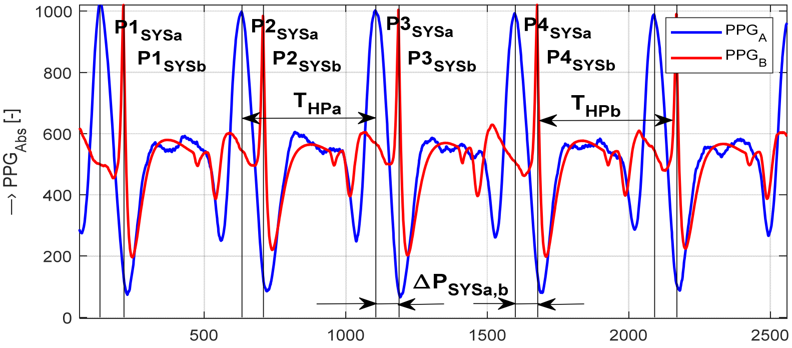

Fig. 1.12. An example of 2.5k-sample parts of two PPG waves sensed in parallel (PPG_A and PPG_B) with denoted heart pulse periods $T_{HPa,b}$ and determined time differences between systolic pulses $\Delta P_{SYSa,b}$.

The final accuracy of the determined PWV values depends partially also on the absolute error of practical measurement of the distances *D*x. The fist optical sensor is usually mounted on a wrist, and the second one on finger(s), so the *D*x distance can be easily measured along the horizontal line as follows from the arrangement photo in Fig. 1.13. More sophisticated method measures the *D*x as a length of the path between the wrist and the fingers along the blood arteries. This methodology follows from the fact that the blood really flows in this way in a measured hand. The main disadvantage of this measurement approach is its great individual-dependence. In addition, the distance *D*x could be finally measured with lower accuracy – practically comparable with the first easy way and will not bring better results.

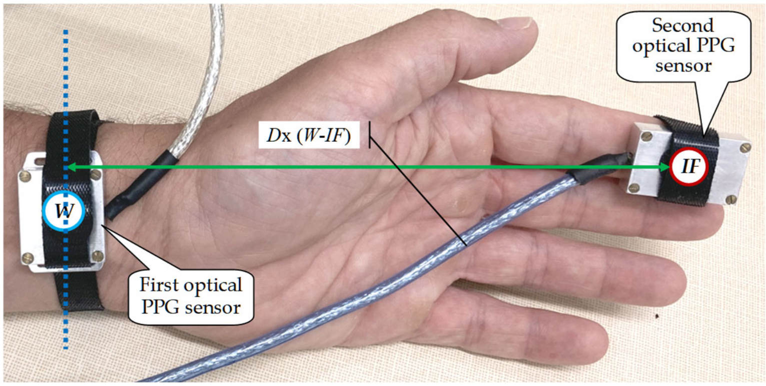

Fig. 1.13. An example of arrangement for two-channel PPG signal acquisition by optical sensors located on a wrist (*W*) and an index finger (*IF*) at a distance *D*x measured along the horizontal line.

The obtained PPG wave parameters are then statistically processed to get one final representative value for direct numerical comparison. The histograms are useful to map and describe distribution of their values. When the probability distribution of the analyzed parameter has non-Gaussian character, then using the mean or median values does not provide a correct final result. In this case it is better to determine the value h_{MAX} corresponding to the maximum occurrence o_{MAX} [%] in the histogram, however, o_{MAX} must be significant – in praxis is usually sufficient to use $o_{\mathrm{MAX}} \geq 20$ %. Otherwise, higher differences between h_{MAX} and mean values are present (as shown by histograms in Fig. 1.14), and better precision is practically achieved by calculation using the median method.

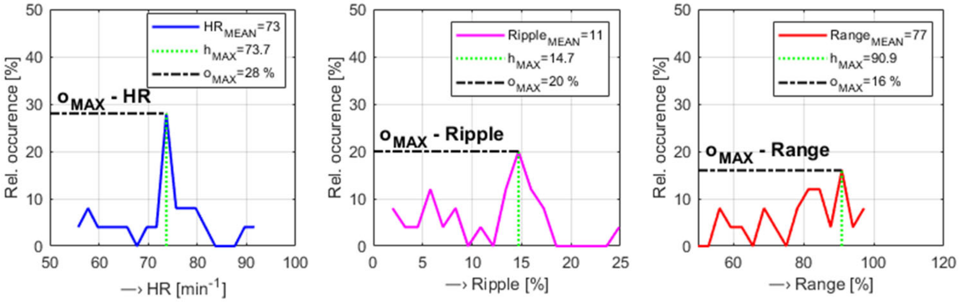

Fig. 1.14. Histograms demonstrating differences between calculated mean and h_{MAX} values in dependence on maximum occurrence o_{MAX} for: HR, systolic peak ripple, and relative signal range parameters (from left to right).

1.4. Evaluation of Precision of Realized PPG Sensors

To evaluate the precision and stability of HR values determined from sensed PPG signals (HR_{PPG}), two types of comparative measurements of HR values (HR_{CMP}) were performed:

1. comparative measurement of HR values determined from PPG signals sensed by three one-channel PPG sensors together with parallel measurement by a certified OXI device;
2. comparison of the accuracy and stability of HR values determined from PPG signals sensed by all five developed wearable PPG sensors – the HR values were measured in parallel by a commercial BPM device used also in medical practice.

When the comparative HR measurement by a BPM device is applied, the HR_{CMP} parameter represents one value HR_{BPM} obtained for the whole measuring interval with duration T_{DUR}. In the case of using an oximeter which produces continual values of HR during the whole measurement, the HR_{OXI} is defined as the mean value. To enumerate the overall estimation accuracy, the percentage relative differential parameter HR_{DIFF} – relative to the mean value of HR_{PPG} sequence (μHR_{PPG}) – can be calculated as

$$HR_{\mathrm{DIFF}} = (HR_{\mathrm{CMP}} - HR_{\mathrm{PPG}}) / \mu HR_{\mathrm{PPG}} \times 100 \tag{1.8}$$

The obtained accuracy is compared with other related works using the mean absolute error (MAE) parameter calculated as a mean of a simple absolute difference $\Delta HR_{\mathrm{OXI,BPM}} = HR_{\mathrm{CMP}} - HR_{\mathrm{PPG}}$ in min^{-1}. For mapping of correlations between the measured HR_{CMP} and the determined HR_{PPG} values, the scatter plots can be used. For this purpose, the Pearson correlation coefficient R is calculated as

$$R(X,Y) = \frac{1}{N-1}\sum_{n=1}^{N} \left((X_n - \mu_X)\ /\sigma_X\right)\cdot\left((Y_n - \mu_Y)\ /\sigma_Y\right), \tag{1.9}$$

where X represents the vector of measured HRs and Y is the vector of HR values determined from PPG waves, μ and σ denote the mean and the standard deviation of the input vectors X and Y consisting of N elements.

The first stage of comparative measurements was realized in the conditions when the PPG signal from the tested prototype of a PPG sensor was sensed on a little finger, and the oximeter Berry BM1000C [40] used in parallel was worn on an index finger. This type of an OXI device works in a transmittance mode and enables transfer and recording of a PPG signal via BT connection to a control device. There are simultaneously calculated and displayed arterial blood oxygen saturation (SpO_2), perfusion index (PI), and HR values – see an experimental arrangement photo in Fig. 1.15a (the tablet Lenovo M10 was used in these measurements). In the second part of comparative measurements, the automatic blood pressure monitor BP A150-30 AFIB by Microlife AG [41] was applied. To prevent negative influence of an inflated pressure cuff of the BPM on a tested person's blood system, the PPG signal was picked up from an index finger of the opposite hand as documented by the arrangement photo in Fig. 1.15b. The PPG signal recording as well as the measurement by an oximeter always lasted with duration T_{DUR} = 80 sec. The evaluation of the HR precision was performed numerically (by the mean HR_{DIFF} values per a PPG sensor prototype), and also graphically using the correlation scatter plots (see graphs in Fig. 1.16) and Bland-Altman plots (see Fig. 1.17).

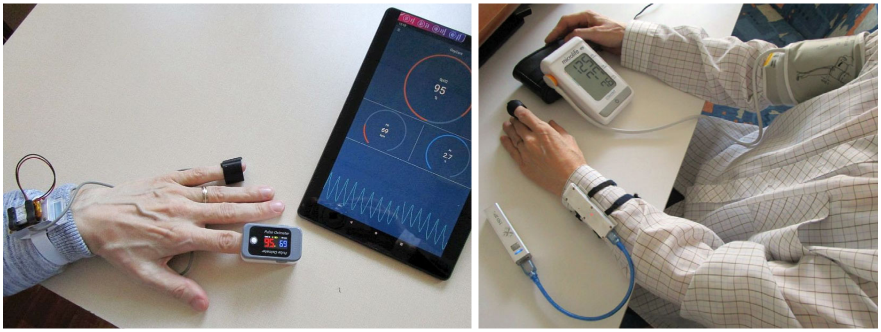

a) b)

Fig. 1.15. Arrangements of comparative measurements: a) Parallel sensing of the PPG signal by the PPG-BLE sensor and via the OXI with BT data transfer to a tablet (both placed on the same hand); b) Parallel HR measurement by the BPM device (pressure cuff on the right arm) and PPG signal sensing by the PPG-PS1 sensor worn on the opposite left hand.

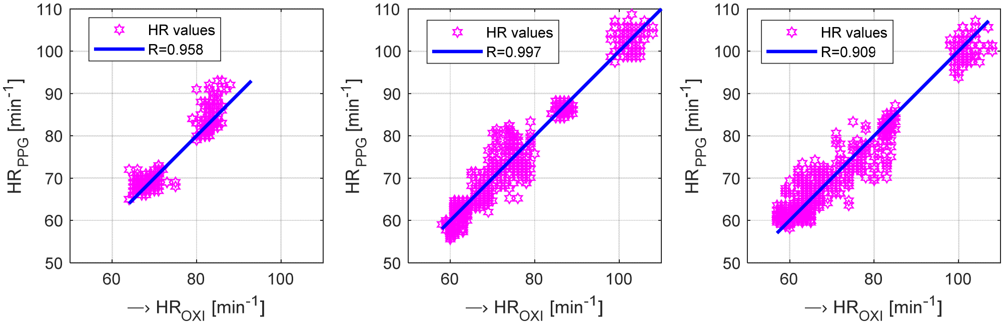

a) b) c)

Fig. 1.16. Scatter plots of correlations between the values measured (HR_{OXI}) and determined from PPG signals (HR_{PPG}) together with the calculated R coefficient using: a) PPG-EP; b) PPG-PS1; c) PPG-BLE sensors.

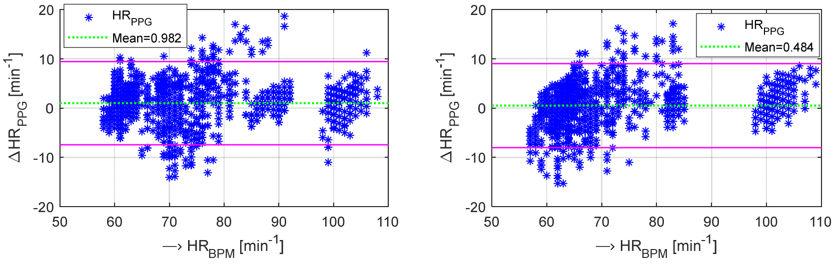

a) b)

Fig. 1.17. Resulting Bland-Altman plots of the HR determination accuracy from PPG waves with parallel HR measurement by a BPM device for: a) PPG-2Tp; b) PPG-3p sensors.

1.5. Conclusions and Future Work

Wearable PPG sensor prototypes described in this study were developed especially for measurement in the weak magnetic field environment. Before starting this development, we had already tested commercial "fitness bracelets" and smart watches. These types of devices work in the reflectance mode and produce HR parameter values that are not very precise and are not designed for function in the conditions of the running MRI tomograph. In addition, majority of these commercial devices are not able to send the PPG signal samples to an external device (the HR values only). For our purpose we need to evaluate fast and slow changes of the heart rate as well as changes in the width of systolic/diastolic pulses to determine special PPG signal properties (for example the Oliva-roztocil index which has been used as an approach to pain quantification [42]). The heart pulse transmission parameters (PTT and PWV) seem to be sufficient for this task. These parameters are successfully usable for stress detection, evaluation, and classification – for mapping and monitoring of these objective clinical states observed in people who are exposed to negative factors for a short period of time – such as during scanning inside the MRI device.

From experimental studies and practical measurements follows that the actual state of the skin surface including a color, a temperature, and other factors have influence on the quality and properties of the sensed PPG signals. Thus, PPG sensors are supplemented by a contact thermometer to carry out the measurement of the skin temperature to map its changes during an experiment. In addition, the precision of the determined PPG wave features depends also on the actual position of the optical sensor and the contact pressure exerted in the place of the sensor. To analyze this influence, force-sensitive resistors (FSR) can be successfully used to measure the localized physical pressure.

For this reason, we plan in the near future to develop a new wearable PPG sensor including also an integrated contact thermometer and an FSR element for contact pressure measurement. Next, for different contact forces on a finger/wrist, we will realize a measurement of PPG signals with the aim to collect a database of PPG wave records. Then, we will analyze the determined PPG wave features to make practical recommendation about setting the contact force which is important for long-time measurement experiments inside the MRI device.

The insufficient precision of manual measurement of distances *D*x can have negative influence on the inaccuracy of PWV values. It could be improved by a semi-automatic approach which is usually used for determination of distances from images.

Finally, we are fully aware that only a small group of tested subjects (typically up to 15 persons) participated in measurement experiments with our developed PPG sensors, so the obtained results and conclusion from the performed observation cannot be generalized. It was caused by several factors and problems. First of all, the open-air MRI device Esaote Opera [9] directly usable for our experiments with PPG signal(s) recording is devised for standard medical practice, and our institute does not hold a certificate for real patient examination. Therefore, it can be used for non-clinical and non-medical research only. We believe that we will be able to establish close cooperation with the nearest medical centers in our country (in Bratislava), Austria (in Vienna), or Czech Republic (Brno, Prague, etc.) to solve this limitation.

Acknowledgements

This work was funded by the Slovak Scientific Grant Agency project VEGA2/0004/23.

References

[1]. L. Schickhofer, J. Malinen, M. Mihaescu, Compressible flow simulations of voiced speech using rigid vocal tract geometries acquired by MRI. *Journal of the Acoustical Society of America*, Vol. 145, 2019, pp. 2049-2061.

[2]. M. Masqsood, F. Nazir, U. Khan, F. Aadil, H. Jamal, I. Mehmood, O. Song, Transfer learning assisted classification and detection of Alzheimer's disease stages using 3D MRI scans, *Sensors*, Vol. 19, 2019, 2645.

[3]. M. Filippi, P. Preziosa, M. A. Rocca, Brain mapping in multiple sclerosis: Lessons learned about the human brain, *NeuroImage*, Vol. 190, 2019, pp. 32-45.

[4]. R. A. Leijendekkers, M. A., Marra, M. J. M. Ploegmakers, G. Van Hinte, J. P. Frölke, H. Van De Meent, N. Verdonschot, Magnetic-resonance-imaging-based three-dimensional muscle reconstruction of hip abductor muscle volume in a person with a transfemoral bone-anchored prosthesis: A feasibility study, *Physiotherapy Theory and Practice*, Vol. 35, Issue 5, 2019, pp. 495-504.

[5]. J. P. Marques, F. J. Simons, A. G. Webb, Low-field MRI: An MR physics perspective, *Journal of Magnetic Resonance Imaging*, Vol. 49, 2019, pp. 1528-1542.

[6]. D. L. Prince, J. P. De Wilde, A. M. Papadaki, J. S. Curran, R. I. Kitney, Investigation of acoustic noise on 15 MRI scanners from 0.2 T to 3 T, *Journal of Magnetic Resonance Imaging*, Vol. 13, 2001, pp. 288-293.

[7]. M. A. Bernstein, K. F. King, X. J. Zhou, Handbook of MRI Pulse Sequences, *Elsevier Academic Press*, Burlington, 2004.

[8]. L. P. Panych, B. Madore, The physics of MRI safety, *Journal of Magnetic Resonance Imaging*, Vol. 47, 2018, pp. 28-43.

[9]. E-Scan Opera, Image Quality and Sequences Manual, Revision 830023522, *Esaote S.p.A.*, Genoa, Italy, 2008.

[10]. J. Přibil, A. Přibilová, I. Frollo, Vibration and noise in magnetic resonance imaging of the vocal tract: differences between whole-body and open-air devices, *Sensors*, Vol. 18, Issue 4, 2018, 1112.

[11]. A. Moelker, P. A. Wielopolski, P. M. T. Pattynama, Relationship between magnetic field strength and magnetic-resonance-related acoustic noise levels, *Magnetic Resonance Materials in Physics, Biology and Medicine*, Vol. 16, 2003, pp. 52-55.

[12]. J. Přibil, A. Přibilová, I. Frollo, Comparison of mechanical vibration and acoustic noise in the open-air MRI, *Applied Acoustics*, Vol. 105, April 2016, pp. 13-23.

[13]. J. Přibil, A. Přibilová, I. Frollo, Comparison of three prototypes of PPG sensors for continual real-time measurement in weak magnetic field, *Sensors*, Vol. 22, Issue 10, 2022, 3769.

[14]. M. C. Steckner, A review of MRI acoustic noise and its potential impact on patient and worker health, *eMagRes*, Vol. 9, 2020, pp. 21-38.

[15]. P. Celka, P. H. Charlton, B. Farukh, P. Chowienczyk, J. Alastruey, Influence of mental stress on the pulse wave features of photoplethysmograms, *Healthcare Technology Letters*, Vol. 7, 2020, pp. 7-12.

[16]. V. Randazzo, J. Ferretti, E. Pasero, A wearable smart device to monitor multiple vital parameters – VITAL ECG, *Electronics*, Vol. 9, 2020, 300.

[17]. A. G. Bonomi, F. Schipper, L. M. Eerikäinen, J. Margarito, R. Van Dinther, G. Muesch, H. M. De Morree, R. M. Aarts, S. Babaeizadeh, D. D. McManus, Atrial fibrillation detection using a novel cardiac ambulatory monitor based on photoplethysmography at the wrist, *Journal of the American Heart Association*, Vol. 7, 2018, e009351.

[18]. J. Sancho, A. Alesanco, J. García. Biometric authentication using the PPG: a long-term feasibility study, *Sensors*, Vol. 18, 2018, 1525.

[19]. B. C. Casadei, A. Gumiero, G. Tantillo, L. Della Torre, G. Olmo, Systolic blood pressure estimation from PPG signal using ANN, *Electronics*, Vol. 11, 2022, 2909.

[20]. Y. J. Wang, C. H. Chen, C. Y. Sue, W. H. Lu, Y. H. Chiou, Estimation of blood pressure in the radial artery using strain-based pulse wave and photoplethysmography sensors, *Micromachines*, Vol. 9, 2018, 556.

[21]. M. Johnson, R. Jegan, X. Mary, Performance measures on blood pressure and heart rate measurement from PPG signal for biomedical applications, in *Proceedings of the IEEE International Conference on Innovations in Electrical, Electronics, Instrumentation and Media Technology (ICEEIMT'17)*, Coimbatore, India, 3-4 February 2017, pp. 311-315.

[22]. Y. Xu, W. Zhang, D. Wang, P. Ping, A calibration method for cuffless continue blood pressure measurement using Gaussian normalized pulse transit time, in *Proceedings of the IEEE International Instrumentation and Measurement Technology Conference (I2MTC'18*), Houston, TX, USA, 14-17 May 2018, pp. 1-5.

[23]. H. Gesche, D. Grosskurth, G. Küchler, A. Patzak, Continuous blood pressure measurement by using the pulse transit time: Comparison to a cuff-based method, *European Journal of Applied Physiol*ogy, Vol. 112, 2012, pp. 309-315.

[24]. B. Mishra, N. Thakkar, Cuffless blood pressure monitoring using PTT and PWV methods, in *Proceedings of the International Conference on Recent Innovations in Signal Processing and Embedded Systems (RISE'17)*, Bhopal, India, 27-29 October 2017; pp. 395-401.

[25]. P. H. Charlton, V. Marozas, Wearable photoplethysmography devices, in Photoplethysmography: Technology, Signal Analysis, and Applications (P. A. Kyriacou, J. Allen, Eds.), *Elsevier*, London, UK, 2022, pp. 401-438.

[26]. M. Nitzan, Z. Ovadia-Blechman, Physical and physiological interpretations of the PPG signal, in Photoplethysmography: Technology, Signal Analysis, and Applications (P. A. Kyriacou, J. Allen, Eds.), *Elsevier*, London, UK, 2022, pp. 319-339.

[27]. E. Mejía-Mejía, J. Allen, K. Budidha, C. El-Hajj, P. A. Kyriacou, P. H. Charlton, Photoplethysmography signal processing and synthesis, in Photoplethysmography: Technology, Signal Analysis, and Applications (P. A. Kyriacou, J. Allen, Eds.), *Elsevier*, London, UK, 2022, pp. 69-145.

[28]. A. G. Smith, Introduction to Arduino: A Piece of Cake, *CreateSpace Independent Publishing Platform*, 2011.

[29]. Arduino UNO R3, https://docs.arduino.cc/hardware/uno-rev3

[30]. Arduino Nano Official Store, http://arduino.cc/en/Main/ArduinoBoardNano

[31]. Using the Arduino Pro Mini 3.3V, https://learn.sparkfun.com/tutorials/using-the-arduino-pro-mini-33v

[32]. Adafruit Metro Mini 328 V2, https://www.adafruit.com/product/2590

[33]. Arduino and Bluetooth Module HC-06, https://www.aranacorp.com/en/arduino-and-bluetooth-module-hc-06/

[34]. MLT-BT05 4.1 Bluetooth Serial Communication Module, https://www.techonicsltd.com/product/mlt-bt05-ble4-0/

[35]. Pulse Sensor Amped Product (Adafruit 1093), World Famous Electronics LLC, Ecommerce Getting Starter Guide, https://pulsesensor.com/pages/code-and-guide

[36]. Crowtail – Pulse Sensor (ER-CT010712P) measure the heart rate of the human, https://rlx.sk/sk/biometric-medical-e-health-sensor-eeg-ekg/5431-crowtail-pulse-sensor-er-ct010712p

[37]. Gravity: PPG Heart Rate Monitor Sensor for Arduino (Analog/Digital). https://www.dfrobot.com/product-1540.html

[38]. Easy Pulse Sensor (Version 1.1), Overview – Embedded Lab, http://embedded-lab.com/blog/easy-pulse-version-1-1-sensor-overview

[39]. Easy Pulse Mikro – A Mikrobus Compatible Pulse Sensor – Embedded Lab, https://www.embedded-lab.com/blog/easy-pulse-mikro/#more-11519

[40]. China Berry Hospital Oxycare Pulse Oximeter for Kids, https://berrymedical.en.made-in-china.com/product/zsuQEvPLsqcJ/Ch

[41]. Microlife BP A150 AFIB, https://www.microlife.cz/produkty/krevni-tlak/automaticke-tlakomery/bp-a150-afib

[42]. J. Pitha, P. Pithova, K. Roztocil, K. Urbaniec, Oliva-roztocil index, specific parameter of vascular damage in women suffering from diabetes mellitus, *Atherosclerosis*, Vol. 263, 2017, e275.

Chapter 2
Linearization and Integerization for Computing Algebraic Matroids

David Ash

2.1. Introduction and Motivation

Algebraic matroids have recently emerged as a powerful tool for analyzing dependencies in biological models, particularly in the context of systems described by differential equations. This interest has been partly driven by emerging biological applications, where complex physiological processes are often modeled mathematically. For example, the BioModels website includes over 1000 manually curated models of such processes [7]. The models on that website often take the form of differential equations where the rate of change of species concentrations takes the form of a mathematical function – often but not always a polynomial – in species concentrations and parameters. In these models, the "species" typically refer to concentrations of molecules such as metabolites, while the "parameters" represent system-specific constants. Unlike species, parameters may lack direct physical observability and can vary significantly across subjects, making them harder to measure or infer. Because parameters are not always tied to directly measurable physical quantities – and may vary between subjects – they are often difficult to infer with confidence.

As these models may represent pathological conditions, it can be useful to determine – for example for diagnosis and other applications – whether a given model is manifest in any given subject. Some of the species concentrations may be easy to determine. Others may not be. This raises a natural question: given constraints on what can be measured, how can one design experiments to distinguish among possible models? Algebraic matroids offer one possible framework for approaching this question. In the language of matroid theory, a "basis" is a maximal subset of species that are algebraically independent – none can be expressed as an algebraic function of the others. If the observed species form such a basis (or a subset thereof), the system allows maximal flexibility, making it harder to rule out a model. But if the observed species include a "circuit" – a minimally dependent

---

David Ash
Real Time Agents Inc, 191 Twinbridge Cir, Pleasant Hill, CA 94523, USA

set – then there may be enough structure to reject the model based on the observed values [14].

Using this approach, it has been shown possible to compute algebraic matroids for a number of models from the BioModels website. These include five different Wnt signaling pathway models. Although Bayesian approaches can be used to determine parameter values, the parameter values so determined are approximate, creating a risk of incorrectly confirming or ruling out a model. Once computed, an algebraic matroid provides parameter-free insights: it encodes the dependencies among species regardless of the specific parameter values for a given subject [10].

Algebraic matroids also find application in signal processing. This has occurred through the use of unit norm tight frames in signal processing. Such frames are used in signal processing when there is a need for redundancy. This enables signal recovery even when some coefficients are lost, but at the potential cost of signal uniqueness. Frames are also used to improve the recovery of signals in such cases [18]. Unit norm tight frames are used in signal processing for compressed sensing. Compressed sensing aims to reconstruct a signal from a small number of measurements, often fewer than the ambient signal dimension, by exploiting signal sparsity. This typically involves solving an underdetermined system, often via optimization techniques [20]. Recent studies suggest that unit-norm tight frames outperform earlier methods – such as Gaussian random matrices – in compressed sensing tasks, particularly in terms of reconstruction stability and mean-squared error [5].

The mathematical structure underlying these frame systems – and the relationships among frame vectors – can be studied using tools from algebraic matroid theory, which capture the algebraic dependencies among frame elements. In particular, the problem of reconstructing a unit norm tight frame from a sparse collection of data turns out to be closely related to the structure of a specific algebraic matroid. In particular the set of all such unit norm tight frames for a given dimensionality has a closely related algebraic matroid whose structure, if known, can help with reconstructing a specific unit norm tight frame. However, the complete characterization of such matroids has so far been achieved only for systems with small dimensionality, highlighting a gap in the literature around scalable methods for computing algebraic matroids. This chapter contributes toward addressing that gap by proposing new algorithmic techniques, with both theoretical and empirical support, though challenges in full generality remain [3].

The Gröbner basis algorithm is a standard symbolic approach for computing algebraic matroids but its doubly exponential complexity makes it impractical for all but the smallest matroids. Alternative algorithms have also been explored. For example, in addition to the limited solution noted above for unit norm tight frames, specific algorithms have been found for the Cayley-Menger algebraic matroid [12] and the algebraic rigidity matroid [13]. Nevertheless, a general and tractable method for computing algebraic matroids remains elusive. This chapter explores several strategies – such as linearization and integerization – to address these limitations and offer new directions for tractable matroid computation.

2.2. Background

We begin with the definition of a matroid. A matroid generalizes the concept of linear independence from linear algebra to a more abstract, combinatorial setting. While there are multiple equivalent definitions, one common formulation presents a matroid as an ordered pair $(F, \mathcal{I})$ where F is a finite set and $\mathcal{I}$ is a collection of subsets of F, called the *independent sets*, satisfying the following properties:

- Every subset of an independent set is independent;
- If A, B are independent sets with $|A| > |B|$, then there exists $x \in A \setminus B$ such that $B \cup \{x\}$ is independent.

We will often talk about *bases* and *circuits* in the context of matroids. A basis is an independent set in the context of a matroid that is also maximal: it is not the proper subset of any other independent set. Likewise a circuit is a dependent (not independent) subset that is also minimal – any proper subset of a matroid is independent.

We next define the notion of algebraic independence and an algebraic matroid. Consider a tuple of variables $\mathbf{X} = (x_1, x_2, \dots, x_n)$ and a tuple of parameters $\mathbf{T} = (t_1, t_2, \dots, t_r)$. Suppose we are given a tuple of polynomials, none of them identically zero, $\mathbf{P} = (p_1, p_2, \dots, p_s)$ where each p_i is in $\mathbb{Q}[x_1, x_2, \dots, x_n; t_1, t_2, \dots, t_r]$, considered as a ring of polynomials over the variables and parameters with rational coefficients. Consider a subset $\mathbf{X_0} \subseteq \mathbf{X}$. Then we say that $\mathbf{X_0}$ is *algebraically independent* if for any tuple of polynomials $(q_1, q_2, \dots, q_s)$:

$$\sum_{i=1}^{s} p_i q_i \in \mathbb{Q}[\mathbf{X_0}] \text{ iff} \sum_{i=1}^{s} p_i q_i \equiv 0 \tag{2.1}$$

For formal treatments of algebraic independence over fields, see also [19, 6], and the matroid-theoretic development in [8]. Algebraic independence is often defined via field extensions: a set of elements in an extension field is algebraically independent over a base field if no nontrivial polynomial relation holds among them. In our case, the base field is $\mathbb{Q}$ and the extension field is the ratio of $\mathbb{Q}[x_1, x_2, \dots, x_n; t_1, t_2, \dots, t_r]$ and the ideal generated by the polynomials in **P**.

The set **X** or, by extension, any finite set of polynomials in $\mathbb{Q}[\mathbf{X}]$, may then be considered to be an algebraic matroid. The bases of the matroid are the maximal algebraically independent subsets of the given variables, and the set of circuits is simply the set of algebraically dependent subsets that are minimal.

One classical approach to computing algebraic matroids relies on Gröbner bases. The tuple of polynomials **P** may be considered to generate an ideal. This tuple forms a Gröbner basis if the ideal generated by their leading monomials equals the ideal generated by the leading monomials of all polynomials in the ideal. Here, a leading monomial is defined with respect to a chosen monomial ordering (e.g. lexicographic or graded reverse lex among others), a key component of Gröbner basis theory discussed in more detail in [4]. A challenge with Gröbner bases is that known algorithms for computing them are doubly exponential in the worst case. This has led to a bias against Gröbner bases which may not be entirely justified. Although intractable in the worst case, Gröbner bases are sometimes much more efficient in practice. Therefore we need to look at the particular area we are applying Gröbner bases to and determine the complexity of the Gröbner basis algorithm in that particular case. This may involve both theoretical and experimental results [1]. Gröbner bases have in fact proven to be useful in computing algebraic matroids. This is, in part, because Gröbner bases help us to solve the ideal membership problem [9]. If the ground set **P** has size at most 18, with polynomials of degree at most 4, Gröbner bases are a competitive approach. However computational tractability tails off considerably once the ground set becomes larger, and alternative approaches such as linearization, proposed by Rosen based on earlier work by Ingleton, and integerization, a technique proposed in earlier work by the author, may offer a more tractable alternative [14].

Several examples of algebraic matroids are explored in [11]. One such algebraic matroid is developed for the Schmitz et al. model considering interactions between β-catenin and DC in the cytoplasm and nucleus [17]. This model consists of a set of differential equations describing the dynamics of this biological system. One such differential equation is the following:

$$C'_{XT} = \delta_{11} X_N T - \delta_{12} C_{XT} \tag{2.2}$$

Here C_{XT} denotes the concentration of β-catenin/TCF, X_N denotes the concentration of free nuclear β-catenin, and T denotes the concentration of TCF. This is one of 11 similar differential equations in this model. To determine steady state for this model, one can set the left hand side (rate of change) to zero, and the set of 11 polynomials on the right then form the tuple of polynomials **P** for this model as described above. The algebraic matroid for this model can then be computed. It turns out to have 19 bases and 45 circuits. This was computed in [11] using Gröbner bases because it is a relatively small model, but this approach becomes increasingly impractical as model size and complexity grow.

2.3. Algorithmic Approaches to Algebraic Matroids

We now proceed to explore several different approaches to computing algebraic matroids algorithmically. Since Gröbner bases are quite key to several of our approaches, we will start with a more rigorous definition of a Gröbner basis. Every Gröbner basis is specific to a particular term order, so we start with term orders. Given $\mathbf{X} = (x_1, x_2, \ldots, x_n)$, the set of terms T is defined to be all ${x_1}^{e_1} {x_2}^{e_2} \ldots {x_n}^{e_n}$ where the e_i's are nonnegative integers. Then a term order $\leq$ on T is defined to be a total order on T satisfying the following conditions [2]:

- $1 \leq t$ for all $t \in T$;
- $t_1 \leq t_2$ implies $t_1 \cdot s \leq t_2 \cdot s$ for all $s, t_1, t_2 \in T$.

For any polynomial $f \in \mathbb{Q}[\mathbf{X}]$, we can then define the **head term** $\mathrm{HT}(f)$, the **head monomial** $\mathrm{HM}(f)$, and the **head coefficient** $\mathrm{HC}(f)$ as follows:

- $\mathrm{HT}(f) = \max(T(f))$;
- $\mathrm{HM}(f) = \max(M(f))$;
- $\mathrm{HC}(f)$ = the coefficient of $\mathrm{HM}(f)$.

Here $T(f)$ denotes the set of terms in f and $M(f)$ denotes the set of monomials in f, where a monomial is a term multiplied by a coefficient. The maximum is then defined over the total order $\leq$ on T. For a set of polynomials $P \subseteq \mathbb{Q}[\mathbf{X}]$, we can similarly define:

$$\mathrm{HT}(P) = \{\mathrm{HT}(f): 0 \neq f \in P\}$$

We can then define a **Gröbner basis** to be any finite subset $G \subseteq \mathbb{Q}[\mathbf{X}]$ with no zero element such that for every $s \in \mathrm{HT}(\mathrm{Id}(G))$, there exists $t \in \mathrm{HT}(G)$ with $t|s$. Additionally, if I is an ideal of $\mathbb{Q}[\mathbf{X}]$, then any **Gröbner basis** G is said to be a **Gröbner basis** of I if $\mathrm{Id}(G) = I$ [2].

The reason why **Gröbner bases** are of interest is that they provide a way of solving the ideal membership problem. We are sometimes interested in establishing whether a polynomial f is in the ideal generated by G, $\mathrm{Id}(G)$. We say that f reduces to h modulo G, and write $f \underset{G}{\rightarrow} h$, if there exist $t \in T(f)$, $s \in T$, and $g \in G$ with $s \cdot \mathrm{HT}(g) = t$, satisfying:

$$h = f - \frac{a}{\mathrm{HC}(g)} \cdot s \cdot g \tag{2.3}$$

Here a is the coefficient of t in f. We can next define the $\xrightarrow[G]{*}$ relation to be the reflexive transitive closure of the $\underset{G}{\rightarrow}$ relation. An equivalent definition of a Gröbner basis is that for all $f \in \mathrm{Id}(G)$, $f \xrightarrow[G]{*} 0$. This essentially gives us an algorithm for determining ideal membership, since once we compute the Gröbner basis for a given ideal, we can apply the definition of reduction to a polynomial to determine if the above condition holds, which guarantees ideal membership [2].

Rosen [14] proposes the use of Gröbner bases as a tool for computing algebraic matroids. However the actual Macaulay2 code he provides for performing this computation does not appear to use the gb function directly for computing Gröbner bases [15]. Moreover in [15] there is no pruning of the search – all possible bases of the matroid are explored exhaustively – meaning it is not likely to scale to larger search spaces. This suggests multiple different approaches for computing algebraic matroids, and what follows is believed to be a new approach pruning the search more effectively.

Ingleton [8] provides us with the starting point for our computations. Following Ingleton, we can define a set of derivations D_1, D_2, …, D_r on all polynomials in $\mathbb{Q}[x_1, x_2, \dots, x_n; t_1, t_2, \dots, t_r]$ such that for q_1, $q_2 \in \mathbb{Q}[x_1, x_2, \dots, x_n; t_1, t_2, \dots, t_r]$ and $q \in \mathbb{Q}$:

- $D_i t_j = \delta_{ij}$;

- $D_i(q_1 + q_2) = D_i q_1 + D_i q_2$;
- $D_i(q_1 q_2) = q_2(D_i q_1) + q_1(D_i q_2)$;
- $D_i q = 0$.

If $\mathbf{X_0} = \{x_{i_1}, x_{i_2}, \dots, x_{i_k}\}$, then we can define a gradient vector $\nabla x_{i_j} = (D_1 x_{i_j}, D_2 x_{i_j}, \dots, D_r x_{i_j})$. Ingleton then provides a theorem that $\mathbf{X_0}$ will be algebraically independent if ∇x_{i_1}, ∇x_{i_2}, …, ∇x_{i_k} are linearly independent. However, there is an important caveat. For Ingleton's result to apply, each of the x_i must be algebraic over $\mathbb{Q}[t_1, t_2, \dots, t_r]$. How can we determine if this holds for a given x_i? Consider the ideal $I = (p_1, p_2, \dots, p_s)$ generated by all the polynomials in **P**. We can use a Gröbner basis calculation to eliminate x_2, x_3, …, x_n. If we are able to do so, then we have established that x_1 is algebraic over $\mathbb{Q}[t_1, t_2, \dots, t_r]$. If we can successfully do this for all x_i then Ingleton's theorem applies. To achieve this we can use different term orders in computing Gröbner bases. Ingleton's theorem also requires that each t_j be an independent transcendental over $\mathbb{Q}$. Determining this can likewise be established by using specific term orders in computing the Gröbner basis. If, for example, we are able to eliminate all of x_2, x_3, …, x_n, then we know that all the t_j's are not independent transcendentals over $\mathbb{Q}$, and we will not be able to apply Ingleton's theorem.

We can use the term order to determine whether any given t_j is a transcendental. Consider two terms u, $v \in T$ defined as follows:

- $u = {x_1}^{d_1} {x_2}^{d_2} \dots {x_n}^{d_n} {t_1}^{e_1} {t_2}^{e_2} \dots {t_r}^{e_r}$;
- $v = {x_1}^{f_1} {x_2}^{f_2} \dots {x_n}^{f_n} {t_1}^{g_1} {t_2}^{g_2} \dots {t_r}^{g_r}$,

Then we define the term order by saying that $u \leq v$ iff either the following holds:

$$\sum_{i=1}^{n} d_i + \sum_{i=1}^{r} e_i - e_j < \sum_{i=1}^{n} f_i + \sum_{i=1}^{r} g_i - g_j, \tag{2.4}$$

or $e_j \leq g_j$ and the following holds:

$$\sum_{i=1}^{n} d_i + \sum_{i=1}^{r} e_i - e_j = \sum_{i=1}^{n} f_i + \sum_{i=1}^{r} g_i - g_j \tag{2.5}$$

This has the effect of making all terms involving only powers of t_j the lowest ranked in the term order. If t_j were algebraic, then there must exist a polynomial in t_j with only rational coefficients in the ideal. The high term of such a polynomial is therefore ranked below any terms involving other x_i or t_i. By the definition and properties of a Gröbner basis, if such a polynomial exists, the Gröbner basis associated with this term order must therefore include a polynomial of similar low rank under the term order – also with only powers of t_j. This gives us the way to determine if t_j is transcendental: we compute the Gröbner basis using the above term order. If it includes a polynomial in just t_j then t_j is algebraic and otherwise it is transcendental. We can call this the **specific Gröbner basis algorithm**.

We can similarly define a term order to determine if all of the t_j's are independent transcendentals. For the same $u, v \in T$ as defined above, we can define the term order by saying that $u \leq v$ iff either of the following conditions hold:

$$\sum_{i=1}^{n} d_i < \sum_{i=1}^{n} f_i, \tag{2.6}$$

or:

$$\sum_{i=1}^{n} d_i = \sum_{i=1}^{n} f_i \text{ and} \sum_{i=1}^{r} e_i \leq \sum_{i=1}^{r} g_i \tag{2.7}$$

This has the effect of making all terms involving only powers of any of the t_j the lowest in term order. As before, the Gröbner basis associated with this term order must include a polynomial with only t_j terms if the ideal itself includes such terms. Therefore, to determine if all the t_j are independently transcendental, we need only compute this Gröbner basis and determine whether it has only t_j terms. We can call this the **general Gröbner basis algorithm**.

We next need to determine which of the x_i terms is algebraic or transcendental. Once we have determined that a given x_i is transcendental, we can move it to the set of transcendentals and then evaluate every other x_i in terms of whether it is algebraic in the growing set of transcendentals. This is explained below in the following algorithm:

- Step 1: Verify, using the general Gröbner basis algorithm, that the t_j's are all independently transcendental.
  - Step 1.1: If they are not, STOP because the t_j's are intended to be independent parameters.
- Step 2: Set R, the set of transcendentals, to be $\{t_1, t_2, \dots, t_r\}$. Set A, the set of algebraics, to be $\{x_1, x_2, \dots, x_n\}$.
- Step 3: For each $a \in A$, using the specific Gröbner basis algorithm, determine whether it is algebraic over $\mathbb{Q}[R]$.
- Step 4: If all $a \in A$ are algebraic over $\mathbb{Q}[R]$, STOP.
- Step 5: Pick one specific $a \in A$ such that a is algebraic over $\mathbb{Q}[R]$. Set R to $R \cup \{a\}$ and set A to $A - \{a\}$.
- Step 6: Go to Step 3.

We can now look at a specific example – namely the Schmitz model from [11] described earlier. In this model, the following are the ODE's – the steady state, as discussed earlier, is determined by setting the LHS for all of these to zero, so the polynomials on the RHS comprise the set **P** for this example:

- $X' = \delta_0 - \delta_1 X + \delta_2 X_n - \delta_5 X Y_a + \delta_6 C_{XY}$;
- $Y_a{}' = -\delta_3 Y_a + \delta_4 Y_{an} - \delta_5 X Y_a + (\delta_6 + \delta_7) C_{XY} - \delta_{15} Y_a + \delta_{16} Y_i$;

- $X_n{}' = \delta_1 X - \delta_2 X_n - \delta_8 X_n Y_{an} + \delta_9 C_{XYn} - \delta_{11} X_n T + \delta_{12} C_{XT}$;
- $Y_{an}{}' = \delta_3 Y_a - \delta_4 Y_{an} - \delta_8 X_n Y_{an} + (\delta_9 + \delta_{10}) C_{XYn}$;
- $C_{XY}{}' = \delta_5 X Y_a - (\delta_6 + \delta_7) C_{XY}$;
- $C_{XYn}{}' = \delta_8 X_n Y_{an} - (\delta_9 + \delta_{10}) C_{XYn}$;
- $T' = -\delta_{11} X_n T + \delta_{12} C_{XT}$;
- $C_{XT}{}' = \delta_{11} X_n T - \delta_{12} C_{XT}$;
- $X_p{}' = \delta_7 C_{XY} - \delta_{13} X_p$;
- $X_{pn}{}' = \delta_{10} C_{XYn} - \delta_{14} X_{pn}$;
- $Y_i' = \delta_{15} Y_a - \delta_{16} Y_i$.

Here, applying the general Gröbner basis algorithm will reveal that all δ_i for $0 \leq i \leq 16$ are transcendentals, as we would expect. Of the remaining indeterminates, which correspond to species, it turns out, apply the specific Gröbner basis algorithm, that nine are algebraic and two are transcendental, which we can take to be T and Y_i using the term order approach described above.

Let's summarize where we find ourselves as we lead into the details of the **linearization** approach originally developed in [8]. The polynomials in **P** include three different classes of variables – when we introduced **P** there were just two such classes, but we need to divide the x_i into those which are independent transcendentals over $\mathbb{Q}[t_1, t_2, \dots, t_r]$ and those which are algebraic. We therefore divide the x_i into two groups: y_1, y_2, …, y_p and z_1, z_2, …, z_q where $p + q = n$ and we are ultimately working over the field $\mathbb{Q}[y_1, y_2, \dots, y_p; z_1, z_2, \dots, z_q; t_1, t_2, \dots, t_r]$. Here:

- The t_i are all independent transcendentals over $\mathbb{Q}$;
- The z_i are all independent transcendentals over $\mathbb{Q}[t_1, t_2, \dots, t_r]$;
- The y_i are all algebraic over $\mathbb{Q}[z_1, z_2, \dots, z_q; t_1, t_2, \dots, t_r]$.

The finite set F over which we define a matroid is then given by $F = \{y_1, y_2, \dots, y_p, z_1, z_2, \dots, z_q\}$, where the bases consist of maximal algebraically independent subsets. To compute the matroid, we start with the **gradient matrix M** which is an $n \times q$ matrix $\mathbf{M} = (m_{ij})$ where:

- $m_{ij} = D_j y_i$ for $1 \leq i \leq p$;
- $m_{ij} = D_j z_{i-p}$ for $p + 1 \leq i \leq n$.

Following [8], here D_j is the unique derivation satisfying $D_j z_i = \delta_{ij}$ for $1 \leq i, j \leq q$. We are then tasked with computing the gradient matrix and note that the $D_j z_i$ are clearly easy to compute, but the $D_j y_i$ may be more difficult to compute. To start with this computation, it will help if we first compute $D_j p_i$ for each polynomial $p_i \in$ **P**. We then claim:

Theorem 1: Each $D_j p_i$ is a linear polynomial in $D_j y_k$ for $1 \leq k \leq p$.

Proof: Each polynomial p_i is a sum of terms, each of which is a product of a rational and some number of individual elements of $\{y_1, y_2, \dots, y_p, z_1, z_2, \dots, z_q; t_1, t_2, \dots, t_r\}$, possibly including repetitions. Applying the D_j operator to each such term will lead to a sum of a set of similar products. Each such product will include at most one $D_j y_k$. Since the sum of a set of linear combinations is itself a linear combination, we are done.

We can then define the **coefficient matrix $\mathbf{C}_j$** to be an $s \times p$ matrix $\mathbf{C}_j = (c_{jik})$ where $c_{jik} = [D_j y_k] D_j p_i$ with the coefficient being taken over the field $\mathbb{Q}[y_1, y_2, \dots, y_p; z_1, z_2, \dots, z_q; t_1, t_2, \dots, t_r]$. We can similarly define the **augmented coefficient matrix $\mathbf{A}_j$** to be an $s \times (p+1)$ matrix $\mathbf{A}_j = (a_{jik})$ where $a_{jik} = c_{jik}$ for $k \leq p$ and $c_{ji(p+1)} = [1] D_j p_i$. We next claim:

Theorem 2: Any two coefficient matrices $\mathbf{C}_m$ and $\mathbf{C}_n$ with $1 \leq m < n \leq p$ will be identical, so $\mathbf{C}_m = \mathbf{C}_n$.

Proof: If a specific term in p_i is of the form $y_k q$ for some other term q, then application of the D_m and D_n operators will give us $D_m(y_k q) = q D_m y_k + y_k D_m q$ and $D_n(y_k q) = q D_n y_k + y_k D_n q$. We note that $[D_m y_k] q D_m y_k = q$ and $[D_n y_k] q D_n y_k = q$. So the coefficients are the same for these terms. By induction we can eventually show that $[D_m y_k] y_k D_m q = [D_n y_k] y_k D_n q$, implying $[D_m y_k] D_m(y_k q) = [D_n y_k] D_n(y_k q)$. Since we can do this for each such term, and the derivation operator is additive, the result follows.

We note that this proof will not apply for the augmented matrices, as there will also be terms of the form $z_m q$. Now $D_m(z_m q) = q D_m z_m + z_m D_m q = q + z_m D_m q$ but $D_n(z_m q) = q D_n z_m + z_m D_n q = z_m D_n q$, so there is a q in the first derivation, but not the second. This affects the coefficient of the constant term and hence the augmented matrix, but not any of the coefficient matrices. We can therefore take $\mathbf{C}$ to be the common coefficient matrix. As we proceed, we will be assuming that for each augmented coefficient matrix $\mathbf{A}_j$, $\operatorname{rank}(\mathbf{A}_j) = \operatorname{rank}(\mathbf{C}) = p$. If this were not the case, it would contradict the assumption we are making that each y_k is algebraic over $\mathbb{Q}[z_1, z_2, \dots, z_q; t_1, t_2, \dots, t_r]$. Later we will offer some guidance as to how to proceed if $\operatorname{rank}(\mathbf{C}) < p$. For the moment, we provide the following conjecture:

Conjecture 1: If $\operatorname{rank}(\mathbf{C}) = p$, then it follows that $\operatorname{rank}(\mathbf{A}_j) = p$ for $1 \leq j \leq q$.

Although this conjecture is offered without proof, it seems plausible to believe because if it were not true, it would imply some additional relation holding amongst the elements of $\{y_1, y_2, \dots, y_p, z_1, z_2, \dots, z_q; t_1, t_2, \dots, t_r\}$ which is unlikely to be a linear combination of the p_i. Even if untrue in general, it seems likely to be true in any situation likely to be encountered in practice.

Given that we are assuming that $\operatorname{rank}(\mathbf{C}) = p$, we can then take a linearly independent set of p rows of $\mathbf{C}$, which we can call $\mathbf{C}_0$, and then compute $\mathbf{B} = \mathbf{C}_0{}^{-1}$. This gives us a $p \times p$ matrix and we also have a $p \times 1$ matrix, $\mathbf{B}_j$, which includes precisely those elements of the rightmost column of $\mathbf{A}_j$ corresponding to the rows of $\mathbf{C}$ we selected in defining $\mathbf{C}_0$. Computing $\mathbf{B}\mathbf{B}_j$ then gives us a $p \times 1$ matrix whose element in row i will be $D_j y_i$. At this point we have the gradient matrix and can proceed with an algorithm for computing the bases and circuits. Note here that each row of the gradient matrix corresponds to either one of the y_k or the z_k. In the algorithm that follows, the potential bases will consist of sets of numbers between 1 and n where the actual basis would be the corresponding set of y_k and z_k:

- Step 1: Set the potential basis set to $\{1\}$.
- Step 2: Determine if the potential basis set corresponds to a linearly independent set of rows of $\mathbf{M}$. If it does, take one of the following actions:
  - If the potential basis set has q elements, record it as an actual basis, and all subsets as linearly independent sets.
  - If the potential basis set has fewer than q elements, augment it with an additional element one greater than its largest element. Go back to Step 2.
- Step 3: Find the largest element of the potential basis set with the property that, if we increment it and remove all larger elements, we could still add larger elements to complete a basis with q elements and all elements at most n. If such an element exists, increment it, remove all larger elements, and go back to Step 2.
- Step 4: If no element was identified in Step 3, STOP.

Using the set of linearly independent sets, including but not limited to bases identified above, we can then compute the set of circuits as follows:

- Step 1: For each linearly independent set identified in the bases algorithm, if it has k elements, list all supersets with exactly $k + 1$ elements as potential circuits.
- Step 2: For each potential circuit, list all subsets with exactly k elements. If all such subsets are linearly independent, but the superset is not, record it as an actual circuit.

Although the linearization approach as described above works, it may be computationally expensive due to the large number of computations required over fields of rational functions over large numbers of variables. As our final proposal for an algorithm, therefore, we will suggest an improvement called integerization. For the integerization approach, we construct a function $F: \mathbb{Q}[y_1, y_2, \dots, y_p; z_1, z_2, \dots, z_q; t_1, t_2, \dots, t_r] \to \mathbb{Q}$ mapping each element of $\{y_1, y_2, \dots, y_p, z_1, z_2, \dots, z_q; t_1, t_2, \dots, t_r\}$ to a unique prime number. For example, we might set $F(y_1) = 11$, $F(y_2) = 13$, and so on. We choose prime numbers to reduce the likelihood that a multiple of one such number will match another number. We then extend this mapping to the entire field as follows:

- $F(q) = q$ for $q \in \mathbb{Q}$;
- $F(u+v) = F(u) + F(v)$;
- $F(uv) = F(u)F(v)$.

We then perform all operations as indicated above but in the space of rational numbers, not rational functions. We note that any combination of rows of the gradient matrix which are linearly independent in the integerized space will still be linearly independent in the original space, although the converse does not necessarily hold. Given that we know the size of any given basis, once we have found a linearly independent set with that number of elements, we know it must form a basis. However, if we find a set of linearly dependent elements, before pruning our search in the above algorithm, we should first verify that the set remains linearly independent even in the original space.

We next work through the Schmitz example we introduced earlier. In the following, the variables algebraic over the smaller fields will be C_{XY}, Y_{an}, X_n, X_{pn}, X, X_p, Y_a, C_{XYn}, C_{XT}. These correspond to the y_k in our framework and will always be referred to in that order, so $y_1 = C_{XY}$, $y_2 = Y_{an}$, and so on. Also $z_1 = Y_i$, $z_2 = T$. We can then compute one of the augmented coefficient matrices, $\mathbf{A_1}$, which corresponds to Y_i, as follows (Fig. 2.1):

$$\begin{bmatrix}
\delta_6 & 0 & \delta_2 & 0 & -\delta_1 - \delta_5 Y_a & 0 & -\delta_5 X & 0 & 0 & 0 \\
\delta_6 + \delta_7 & \delta_4 & 0 & 0 & -\delta_5 Y_a & 0 & -\delta_3 - \delta_5 X - \delta_{15} & 0 & 0 & \delta_{16} \\
0 & -\delta_8 X_n & -\delta_2 - \delta_8 Y_{an} - \delta_{11} T & 0 & \delta_1 & 0 & 0 & \delta_9 & \delta_{12} & 0 \\
0 & -\delta_4 - \delta_8 X_n & -\delta_8 Y_{an} & 0 & 0 & 0 & \delta_3 & \delta_9 + \delta_{10} & 0 & 0 \\
-\delta_6 - \delta_7 & 0 & 0 & 0 & \delta_5 Y_a & 0 & \delta_5 X & 0 & 0 & 0 \\
0 & \delta_8 X_n & \delta_8 Y_{an} & 0 & 0 & 0 & 0 & -\delta_9 - \delta_{10} & 0 & 0 \\
0 & 0 & -\delta_{11} T & 0 & 0 & 0 & 0 & 0 & \delta_{12} & 0 \\
0 & 0 & \delta_{11} T & 0 & 0 & 0 & 0 & 0 & -\delta_{12} & 0 \\
\delta_7 & 0 & 0 & 0 & 0 & -\delta_{13} & 0 & 0 & 0 & 0 \\
0 & 0 & 0 & -\delta_{14} & 0 & 0 & 0 & \delta_{10} & 0 & 0 \\
0 & 0 & 0 & 0 & 0 & 0 & \delta_{15} & 0 & 0 & -\delta_{16}
\end{bmatrix}$$

Fig. 2.1. Augmented coefficient matrix for Schmitz model.

Per our approach, we can then make the following integer assignments (Fig. 2.2):

$$\begin{array}{ccccccc}
\delta_0 = 43 & \delta_1 = 47 & \delta_2 = 53 & \delta_3 = 59 & \delta_4 = 61 & \delta_5 = 67 & \delta_6 = 71 \\
\delta_7 = 73 & \delta_8 = 79 & \delta_9 = 89 & \delta_{10} = 11 & \delta_{11} = 19 & \delta_{12} = 13 & \delta_{13} = 31 \\
\delta_{14} = 23 & \delta_{15} = 41 & \delta_{16} = 37 & C_{XY} = 17 & Y_{an} = 29 & X_n = 97 & X_{pn} = 101 \\
X = 103 & X_p = 107 & Y_a = 109 & C_{XYn} = 127 & C_{XT} = 131 & Y_i = 113 & T = 83
\end{array}$$

Fig. 2.2. Integer assignments for Schmitz model.

After making these integer assignments, the augmented coefficient matrix can be reduced to the following (Fig. 2.3):

$$\begin{bmatrix}
71 & 0 & 53 & 0 & -7350 & 0 & -6901 & 0 & 0 & 0 \\
144 & 61 & 0 & 0 & -7303 & 0 & -7001 & 0 & 0 & 37 \\
0 & -7663 & -3921 & 0 & 47 & 0 & 0 & 89 & 13 & 0 \\
0 & -7724 & -2291 & 0 & 0 & 0 & 59 & 100 & 0 & 0 \\
-144 & 0 & 0 & 0 & 7303 & 0 & 6901 & 0 & 0 & 0 \\
0 & 7663 & 2291 & 0 & 0 & 0 & 0 & -100 & 0 & 0 \\
0 & 0 & -1577 & 0 & 0 & 0 & 0 & 0 & 13 & 0 \\
0 & 0 & 1577 & 0 & 0 & 0 & 0 & 0 & -13 & 0 \\
73 & 0 & 0 & 0 & 0 & -31 & 0 & 0 & 0 & 0 \\
0 & 0 & 0 & -23 & 0 & 0 & 0 & 11 & 0 & 0 \\
0 & 0 & 0 & 0 & 0 & 0 & 41 & 0 & 0 & -37
\end{bmatrix}$$

Fig. 2.3. Augmented coefficient matrix for Schmitz model after integerization.

Using these values, we can solve for the entries in the gradient matrix, and go on as above to compute the matroid, which has 19 bases and 45 circuits.

2.4. Results and Conclusions

Complete empirical results are not yet available, but we have found some promising preliminary results based on two models – namely the Schmitz model, which we used as an example in Section 3, and the Lee model, also referenced in [11]. We compared our integerization approach to the results obtained by using the code provided in [15]. The initial results are quite promising (Fig. 2.4):

Model	**Integerization**	**Classical**
Schmitz	0.4 sec	0.8 sec
Lee	1.5 sec	20.0 sec

Fig. 2.4. Integerization vs classical approach.

As can be seen, when run on the quite simple Schmitz model, we already see a modest improvement. When we move to the slightly more complex Lee model, however, the improvement grows to over an order of magnitude. One would like to provide a more extensive set of results, comparing results in various scenarios – using Gröbner bases, linearization, integerization, and possible variants of these approaches. Several factors make a complete analysis challenging at this time. Despite the interest in algebraic matroids, it is not clear that anyone has, as yet, provided a complete analysis of a well defined algorithm for doing so. The present work may be one of the first efforts to do so. For example, [10] proposes linearization as an improvement upon Gröbner bases for computing algebraic matroids, but the details of the algorithms for either approach is not included.

The code, provided as a supplement to [15], does work to compute algebraic matroids. The approach in the actual code, however, seems to be to first compute rank, and then loop through all possible subsets of the set of algebraic variables of the appropriate size to determine which represent bases. This likely partially explains why the improvement using the present approach is much greater for the Lee model than for the Schmitz model. The present approach prunes the search. However with the Schmitz model each basis has only two elements, meaning there is no actual pruning to be done. The fact that the present approach still wins, even with the Schmitz model, indicates that pruning is not the only advantage, and the integerization approach itself provides some advantage. However the pruning of the search likely accounts for some of the additional advantage seen with the Lee model.

In the previous section we assumed that $\operatorname{rank}(\mathbf{C}) = p$, and left aside what to do if $\operatorname{rank}(\mathbf{C}) < p$. If $\operatorname{rank}(\mathbf{C}) < p$, then we can reduce $\mathbf{C}$ to row reduced echelon form. Indeed this gives us a possible approach for dividing the x_k into the y_k and z_k. We first compute $\mathbf{C}$ over the x_k. If we find $\operatorname{rank}(\mathbf{C}) < p$, then we compute $\mathbf{C}$ in row reduced echelon form. The columns without leading ones, of which there should be $p - \operatorname{rank}(\mathbf{C})$, correspond to individual x_k. We propose that we treat the x_k corresponding to columns with leading ones as algebraic, and put them in the y_k grouping, and treat the remaining x_k as independent transcendentals over $\mathbb{Q}[t_1, t_2, \dots, t_r]$, putting them in the z_k grouping. In every example we have tried so far, this approach has worked, but we have not yet proven its validity, so we must leave the following as a conjecture:

Conjecture 2: If $\operatorname{rank}(\mathbf{C}) < p$, we can express $\mathbf{C}$ in row reduced echelon form, **E**. We can treat the columns of **E** with leading ones as corresponding to independent transcendentals over $\mathbb{Q}[t_1, t_2, \dots, t_r]$, and the remaining columns as corresponding to algebraics.

Essentially Ingleton [8] gives us a way of determining algebraic independence by instead looking at linear independence over the field extension $\mathbb{Q}[y_1, y_2, \dots, y_p; z_1, z_2, \dots, z_q; t_1, t_2, \dots, t_r]$. The approach we are proposing essentially allows us, in many but potentially not all cases, to reduce this further to looking at linear independence over $\mathbb{Q}$. As we discussed earlier, in some cases we do need to perform a verification step to make sure this reduction has produced a valid result in our particular case. A recent arXiv preprint by Rosen et.al. [16] looks at the intermediate question of whether we can reduce the question to one of linear independence over $\mathbb{Q}[t_1, t_2, \dots, t_r]$. The conclusion of Rosen is that this is definitely not possible in all cases, but promisingly appears to be possible in many cases, although Rosen has not fully characterized the circumstances in which this may be possible.

While the empirical comparisons presented here suggest clear advantages to linearization and integerization, several questions remain open, both in terms of sharpening recent results and extending the theoretical framework; these are taken up in the concluding section on future work.

2.5. Future Work

The present chapter has introduced linearization and integerization as complementary strategies for computing algebraic matroids more efficiently. Integerization, in particular, enables one to identify isomorphic matroids over smaller fields, thereby reducing the computational complexity in many instances. Linearization, while discussed by Rosen, has not previously been developed into a complete algorithm to the best of the author's knowledge; here, it is formalized and then positioned as the foundation for integerization. Together, these methods lay the groundwork for both more scalable algorithms and a more rigorous theoretical framework than has been available in the literature to date.

While the early work of Rosen and his co-authors ([10, 11, 14, 15]) provided a pioneering bridge between algebraic matroids and applied domains such as biology, much of the code provided as a supplement has relied on brute-force enumeration based on Macaulay2 computations. This has left several theoretical and algorithmic questions only partially addressed. In this respect, the present chapter clarifies the exact role of Gröbner bases in the computation of algebraic matroids and connects them explicitly to linearization and integerization, offering a more systematic foundation for further research.

At the same time, the more recent contributions of Rosen, Sidman and Theran [16] may provide a promising framework for removing more of the bottlenecks associated with Gröbner basis computations, provided the results can be sharpened and extended. Integrating those insights with the linearization and integerization framework presented here could yield hybrid approaches that improve both theoretical guarantees and practical performance. This interplay between recent advances and the methods introduced in this chapter points to a particularly fertile line of future investigation.

Finally, there remain deeper questions that reach beyond the immediate computational challenges. Conjectures about the theoretical limits of linearization and integerization, and even connections to foundational propositions such as Zorn's Lemma for infinite analogues, all suggest potential directions for a more abstract mathematical treatment. Such explorations may be of less direct relevance to the signal processing audience of this volume, but they are vital stepping stones toward a broader understanding of algebraic matroids. In this way, the current chapter aims both to advance applied computation and to signal new opportunities for more purely mathematical inquiry.

References

[1]. M. Bardet, J.-C. Faugère, B. Salvy, On the complexity of the F5 Gröbner basis algorithm, *Journal of Symbolic Computation*, Vol. 70, 2015, pp. 49-70.

[2]. T. Becker, V. Weispfenning, Gröbner Bases: A Computational Approach to Commutative Algebra, *Springer*, New York, 1993.

[3]. D. I. Bernstein, C. Farnsworth, J. I. Rodriguez, The algebraic matroid of the finite unit norm tight frame (funtf) variety, *Journal of Pure and Applied Algebra*, Vol. 224, Issue 8, 2020, 106342.

[4]. B. Buchberger, An algorithm for finding the basis elements of the residue class ring modulo a zero-dimensional polynomial ideal, PhD Thesis, *Universität Innsbruck*, Innsbruck, 1966 (in German).

[5]. W. Chen, M. R. D. Rodrigues, I. J. Wassell, On the use of unit-norm tight frames to improve the average MSE performance in compressive sensing applications, *IEEE Signal Processing Letters*, Vol. 19, Issue 1, 2012, pp. 8-11.

[6]. D. A. Cox, J. Little, D. O'Shea, Ideals, Varieties, and Algorithms: An Introduction to Computational Algebraic Geometry and Commutative Algebra, *Springer*, New York, 2015.

[7]. EMBL-EBI, BioModels database, https://www.ebi.ac.uk/biomodels

[8]. A. W. Ingleton, Representation of matroids, in Combinatorial Mathematics and its Applications (D. J. A. Welsh, Ed.), *Academic Press*, London/New York, 1971, pp. 149-167.

[9]. M. Gallinger, Gröbner Bases: Ideal Membership and Graph Colouring, Honours Thesis, *Lakehead University*, Thunder Bay, 2013.

[10]. A. L. MacLean, Z. Rosen, H. M. Byrne, H. A. Harrington, Parameter-free models distinguish Wnt pathway models and guide design of experiments, *Proceedings of the National Academy of Sciences*, Vol. 112, Issue 9, 2015, pp. 2652-2657.

[11]. A. L. MacLean, Z. Rosen, H. M. Byrne, H. A. Harrington, Supporting information for: Parameter-free models distinguish Wnt pathway models and guide design of experiments, 2015, https://pmc.ncbi.nlm.nih.gov/articles/instance/4352827/bin/pnas.1416655112.sapp.pdf

[12]. G. Malić, I. Streinu, Faster algorithms for circuits in the Cayley-Menger algebraic matroid, *arXiv preprint*, 2021, arXiv:2111.14307.

[13]. G. Malić, I. Streinu, Computing circuit polynomials in the algebraic rigidity matroid, *SIAM Journal on Applied Algebra and Geometry*, Vol. 7, Issue 2, 2023, pp. 345-385.

[14]. Z. Rosen, Algebraic Matroids in Applications, PhD Thesis, *University of California-Berkeley*, Berkeley, 2015.

[15]. Z. Rosen, Supplemental material (matroids.m2), GitHub repository, 2015, https://github.com/zvihr/algebraic-matroids/blob/master/matroids.m2

[16]. Z. Rosen, J. Sidman, L. Theran, Linearizing algebraic matroids, *Advances in Mathematics*, Vol. 430, 2023, 109214.

[17]. Y. Schmitz, K. Rateitschak, O. Wolkenhauer, Analysing the impact of nucleo-cytoplasmic shuttling of β-catenin and its antagonists APC, Axin and GSK3 on Wnt/β-catenin signaling, *Cellular Signalling*, Vol. 25, Issue 11, 2013, pp. 2210-2221.

[18]. E. V. Tsiligianni, L. P. Kondi, A. K. Katsaggelos, Construction of incoherent unit norm tight frames with application to compressed sensing, *IEEE Transactions on Information Theory*, Vol. 60, Issue 4, 2014, pp. 2319-2330.

[19]. B. L. van der Waerden, *Algebra, Vol. 1*, *Frederick Ungar Publishing Company*, New York, 1970 (English edition).

[20]. P. Zhang, L. Gan, S. Sun, C. Ling, Modulated unit-norm tight frames for compressed sensing, *IEEE Transactions on Signal Processing*, Vol. 63, Issue 15, 2015, pp. 3974-3985.

Chapter 3

Holotomography Approach for the Detection and Segmentation of Amoebas in Water Samples Using Active Contour

Anass Cherkaoui, Abdelaziz Essadike and Abdenbi Bouzid

3.1. Introduction

Holotomography is a technique that combines holography with tomography to create cross-sectional images of an object [1]. It involves capturing multiple holograms from different angles and using computer algorithms to reconstruct a three-dimensional image of the object [2]. This allows for detailed analysis of the object's internal structure and can be used to visualize objects that are transparent or otherwise difficult to image using other methods [3]. In biology, holographic tomography has been used to study the internal structure of cells and other biological samples, such as visualizing the three-dimensional structure of cells and their organelles and tracking the movement of molecules within cells. Overall, holographic tomography is a valuable tool for studying the internal structure of objects and has a variety of applications in biology and other fields.

Amoebas are a type of single-celled organism that are found in a variety of aquatic environments, including freshwater, marine, and soil. While most amoebas do not pose a significant threat to humans, some types of amoebas can cause serious infections if they enter the human body through the nose, mouth, or other openings. For example, the amoeba Naegleria fowleri, which is commonly found in warm freshwater environments, can cause a rare and often fatal brain infection called primary amebic meningoencephalitis (PAM) if it is inhaled through the nose. In addition to the dangers posed to humans, some types of amoebas can also be harmful to other aquatic organisms and can affect the overall quality of the water. It is important to be aware of the potential risks associated with amoebas and to take appropriate precautions to avoid exposure. Amoebas are a type of eukaryotic organism that are traditionally classified under the Kingdom Protista. They are characterized by their ability to change shape, a trait that is facilitated by their flexible cell

---

Anass Cherkaoui
Hassan I University, Faculty of Science and Technology, Higher Institute of Health Sciences, Settat, Morocco

walls. Some amoebas, such as Naegleria fowleri, are capable of entering the human body through the nose and feeding on neurons, leading to destruction of brain tissue. This type of amoeba is often referred to as the brain-eating amoeba, and it has a very high fatality rate of 97 %. It is important to be aware of the potential risks posed by this type of amoeba [4, 5].

Holotomography is a technique that combines holography with tomography (a method for creating cross-sectional images of an object) to create detailed, three-dimensional images of objects [2, 7]. It involves capturing multiple holograms of an object from different angles and using computer algorithms to reconstruct a three-dimensional image of the object's internal structure and properties [8]. Holographic tomography has a wide range of applications, including the study of biological samples such as cells and microorganisms [9, 10], as well as non-biological objects such as materials and engineering structures [11]. One of the key advantages of holographic tomography is that it is non-invasive and does not require the use of stains or chemical agents, making it a safe and reliable method for studying objects in their natural state [5]. In this paper, we will describe our use of holographic tomography to extract and segment amoebas from liquids.

The study of amoebas, single-celled organisms that are found in a variety of aquatic environments, is of great interest due to their diverse roles in ecosystems and their potential impacts on human health [1]. To accurately and precisely study the behavior and characteristics of amoebas, it is important to be able to extract and segment them from liquids, such as water samples. In this study, we used holographic tomography, a technique that involves capturing multiple holograms of an object from different angles and using computer algorithms to reconstruct a three-dimensional image [12], to extract and segment amoebas from liquids. By analyzing the three-dimensional images of the amoebas, we were able to study their size, shape, and movement in detail [9]. Holographic tomography is a non-invasive technique that does not require the use of stains or chemical agents, making it a safe and reliable method for studying amoebas in their natural habitat [12]. In this paper, we will describe our use of holographic tomography to extract and segment amoebas from liquids and discuss the benefits of this approach.

Overall, the use of holotomography technique to extract and segment amoebas from liquids allows for detailed, three-dimensional analysis of these organisms and can provide valuable insights into their behavior and characteristics. By visualizing and tracking the movement of amoebas in real-time, it is possible to study their interactions with their environment and understand how they may be affected by different factors. Additionally, the non-invasive nature of holographic tomography makes it a safe and reliable method for studying amoebas in their natural habitat. In the following sections, we will present our results and discuss the implications of our findings for the study of amoebas and their role in ecosystems and human health.

3.2. Materials and Methods

3.2.1. Experimental Setup

In our experimental setup, we harnessed the technique of holotomography to examine water samples containing amoebas. We initiated the process with a sophisticated doubled YAG laser, operating at a precise wavelength of 532 nm, characterized by an ultra-short pulse width of 10 nanoseconds and an impressive pulse energy of 100 millijoules. This powerful laser system played a pivotal role in capturing holograms of our water samples, with a unique twist. Rather than employing a traditional single-angle holography approach, we took a multi-angle approach. We recorded holograms at six specific angles: 0°, 30°, 60°, 90°, 120°, and 150°. This multi-angle strategy was instrumental in enhancing our holographic recordings by providing a comprehensive view of the amoebas within the water samples. It significantly boosted both the resolution and contrast of our holographic imagery. The key advantage of employing a pulsed laser in our setup lay in its ability to eliminate motion blur. As we recorded the dynamic water droplets containing amoebas, the pulsed laser's ultra-short duration ensured that even rapidly moving objects were imaged with precision, guaranteeing accuracy in the representation of amoebas. Subsequent to hologram acquisition, we took a post-processing approach. We meticulously extracted the phase component for each recorded slice based on our previous work [13-21]. The purpose of this phase extraction was to isolate the characteristic features of the amoebas. To achieve this, we turned to active contour theory. This advanced image segmentation technique proved highly effective in distinguishing the amoebas from the background, substantially enhancing the interpretability of the holographic data. Now, the heart of our approach lay in the application of holotomography. This technique allowed us to reconstruct detailed three-dimensional structural information and study the dynamic behaviors of the amoebas with an exceptional degree of precision. Holotomography, with its capacity for volumetric reconstruction, provided invaluable insights into the amoebas' morphology and their interactions within their aquatic environment. Lenses in our setup were instrumental in precisely directing and focusing the laser beam, ensuring optimal beam quality. Furthermore, a beam splitter and six CCD cameras, each equipped with its own lens, facilitated simultaneous hologram recording from multiple angles, enabling comprehensive imaging of amoebas within water samples. In summary, our experimental setup, which seamlessly integrated holotomography with a high-powered pulsed laser, multi-angle holographic recording, and advanced image segmentation techniques, enabled us to effectively extract and segment amoebas from water samples. This comprehensive approach offered a profound understanding of amoeba behavior, their intricate three-dimensional structure, and their interactions within their aquatic habitat, thus advancing our scientific analysis in the field.

3.2.2. Detection Phase

Fig. 3.2 showcases inline holograms of water samples containing amoebas recorded at various angles (0 degrees, 30 degrees, 60 degrees, 90 degrees, 120 degrees, and

150 degrees) using our experimental setup. These holograms were instrumental in our endeavor to detect the presence of amoebas through the phase component.

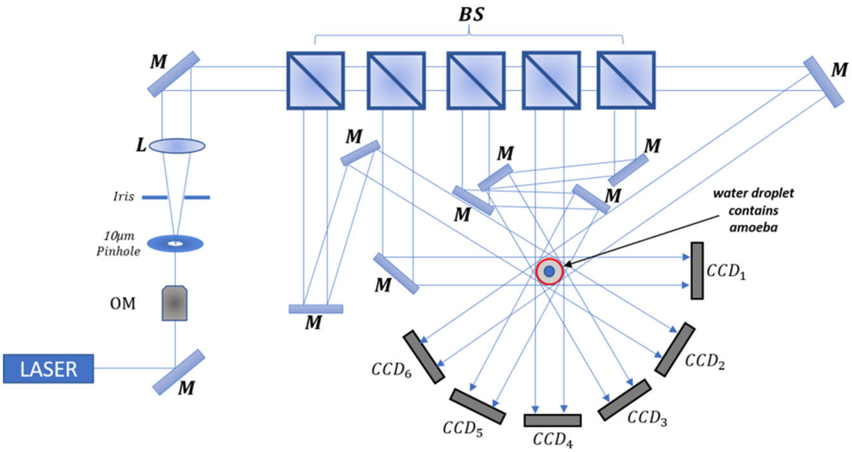

Fig. 3.1. Holotomography Setup for the detection Amoebas from Liquids samples.

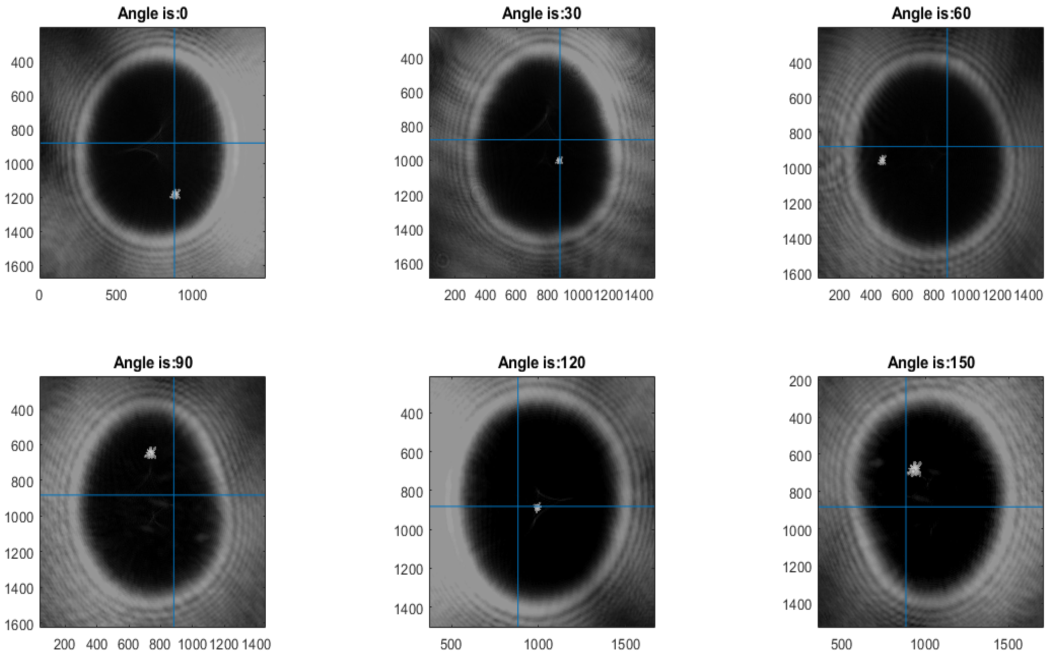

Fig. 3.2. Recorded Inline Holograms of Water Samples Containing Amoebas.

To elaborate on the scientific aspect, the detection of amoebas relied on the variation in the phase component caused by the refractive index differences between the amoebas and their surrounding water medium. The extraction of the phase component for each recorded slice provided valuable data regarding these refractive index disparities, ultimately enabling the identification and localization of amoebas within the holograms. This phase-based detection approach not only offers high sensitivity but also allows for label-free and non-destructive analysis, making it a powerful tool in the realm of biological imaging and analysis.

The integration of holotomography with phase extraction techniques in our study represents a cutting-edge approach to the detection of amoebas in water samples. Holotomography provided us with the capability to acquire detailed three-dimensional information about the specimens. This technique was instrumental in capturing inline holograms from multiple angles, giving us a comprehensive view of the amoebas within the samples. Concurrently, phase extraction served as the key to unveil the amoebas within the holographic data.

Through phase extraction [15], we deciphered the specific phase changes induced by the presence of amoebas in the laser light. These phase variations were intricately linked to refractive index differences between the amoebas and the surrounding water medium. By combining holotomography and phase extraction, we could localize amoebas with a high degree of precision, leveraging the remarkable sensitivity of phase-based detection. The resulting combination allowed us to not only observe the three-dimensional structure of the amoebas but also accurately pinpoint their positions within the samples. This synergy between holotomography and phase extraction represents a significant advancement in biological imaging, providing a holistic approach for the detection, localization, and detailed study of amoebas in their natural aquatic habitat.

In Fig. 3.3, we delve into the critical phase of detection in our holographic tomography setup. This phase illustrates the results of our method applied to all the recorded slices at different angles. The primary objective here is to showcase the effectiveness and reliability of our proposed approach for detecting amoebas within liquid samples using our system. To understand this process scientifically, consider the object of interest as a small 3D structure situated at a distance "d" from the CCD camera. In our holographic tomography setup, we employ the Fresnel approximation formula, a well-established mathematical approach in optics. The core of this method involves utilizing an inverse Fourier-transform formula, as expressed in Equation (3.1). This mathematical procedure allows us to computationally reconstruct the holograms recorded at different angles, thereby generating a comprehensive view of the object's three-dimensional characteristics. In this case, it enables us to visualize and analyze the presence and location of amoebas within the liquid samples with a high degree of accuracy, highlighting the robustness of our detection method.

$$\begin{aligned}\Gamma(\xi,\eta) &= j\frac{1}{\lambda d} exp\left(-j\frac{2\pi d}{\lambda}\right) exp\left[-j\frac{\pi}{\lambda d}(\xi^2+\eta^2)\right]\times \\ &\times \int_{-\infty}^{+\infty}\int_{-\infty}^{+\infty} h(x,y)\, E_R^*(x,y) exp\left[-j\frac{\pi}{\lambda d}(x^2+y^2)\right]\times \\ &\times exp\left[j\frac{2\pi}{\lambda d}(x\xi+y\eta)\right] dxdy =\equiv \hat{z}(\xi,\eta)\Im_{x,y}[hE_R^* w]|_{k_x=2\pi\xi/\lambda d, k_x=2\pi\eta/\lambda d},\end{aligned} \tag{3.1}$$

where $\Im_{x,y}[hE_R^* w]$ is the Fourier transform operator. The intensity is calculated by squaring the optical field, i.e., $I(\xi,\eta) = |\Gamma(\xi,\eta)|^2$, and the phase is calculated using $\phi(x,y) = \arctan\,(Im[\Gamma(\xi,\eta)]Re[\Gamma(\xi,\eta)]$. If x, y are discretized on a rectangular raster of $N_x, \times N_y$ points (corresponding to the number of pixels in the CCD camera in the x and y dimensions, respectively) with step sizes Δx, Δy, which are the pixel-to-pixel distances on the CCD in the x and y directions, respectively.

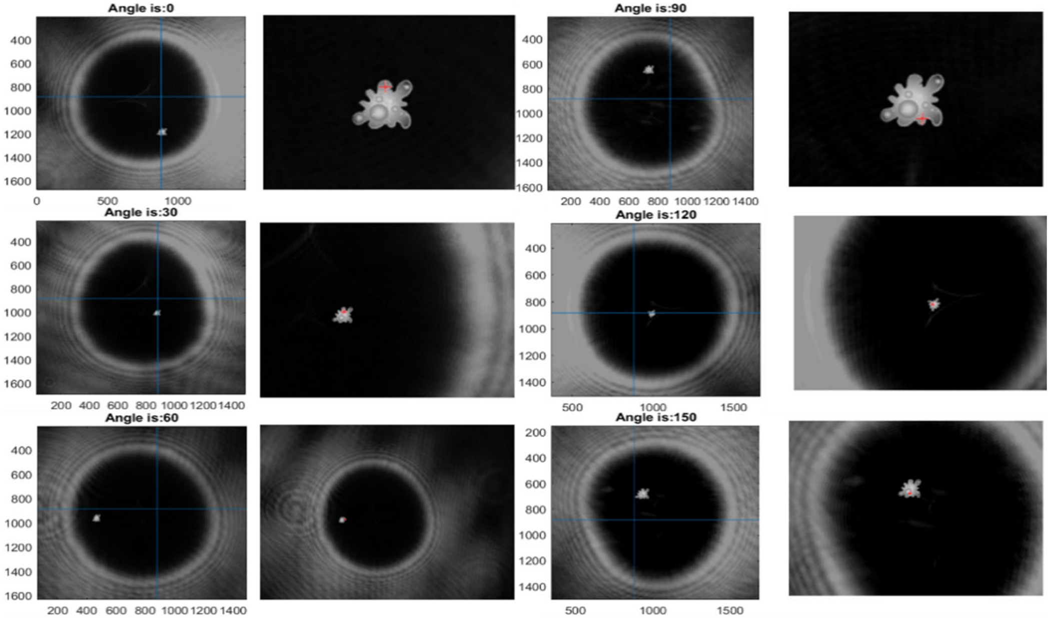

Fig. 3.3. Holographic Detection of Amoebas: Phase Analysis at Diverse Angles.

Fig. 3.4 provides a visual representation of the distribution of phase component peaks at amoeba positions according to the proposed method. These peaks, crucial for identifying amoeba presence, are recognized using our method and clearly highlighted in the figure using the red color. This distribution map facilitates a comprehensive comparison of phase values across various angles, underscoring the efficacy of our proposed technique for reliable amoeba detection and segmentation in liquid samples. In a manner similar to its application in our study [15, 19], Fig. 3.4 underscores the importance of parameter "L" as a reliable indicator for amoeba detection within the liquid medium. It's worth noting that in the case of amoebas, the average L value in our healthy water sample images stands at 130, while in water samples contain amoebas, it significantly rises to 427. Moreover, the in-phase component peaks consistently fall within the [400, 450] range for amoebas, highlighting their presence. Conversely, in images of healthy water samples with uniform pixel intensity distribution, the in-phase component peaks remain confined to the [110, 150] range.

Fig. 3.5a presents the 3D reconstruction of amoebas in liquids using our proposed setup. The figure includes multiple views of the reconstructed 3D image, including top, bottom, front, and side views. This figure provides a detailed and comprehensive view of the 3D structure of the amoebas and allows for the visualization of their internal features. this figure helps to illustrate the capabilities of our proposed setup for 3D reconstruction of sample of water. this figure helps to illustrate the capabilities and potential of our proposed setup for 3D reconstruction. The Fig. 3.5b provides a detailed and comprehensive view of the multiple projections of the volume from different angles and allows for the visualization of the internal features and relationships within the volume.

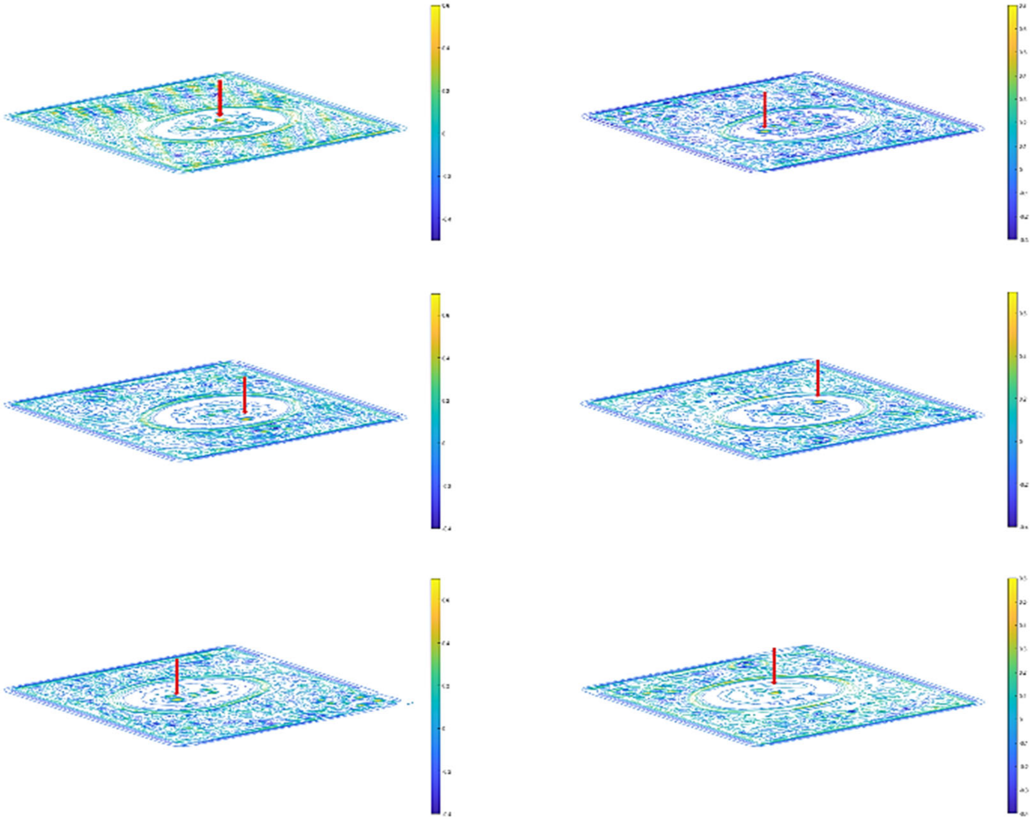

Fig. 3.4. Phase component peaks at the amoeba position according to the proposed method.

After the initial contour has been optimized using the proposed active contour model, the 3D shape of the object can be reconstructed by numerically reconstructing the function $h(x, y)$ and computing the intensities I on multiple planes at various angles and at distance d surrounding the test volume. This process involves using the discretized form of the Fresnel diffraction formula and performing some coordinate transformations. The resulting reconstructed intensities are then multiplied along each angular projection to obtain a 3D reconstruction of the object Equation (3.2).

$$I = \prod_1^M I_j \tag{3.2}$$

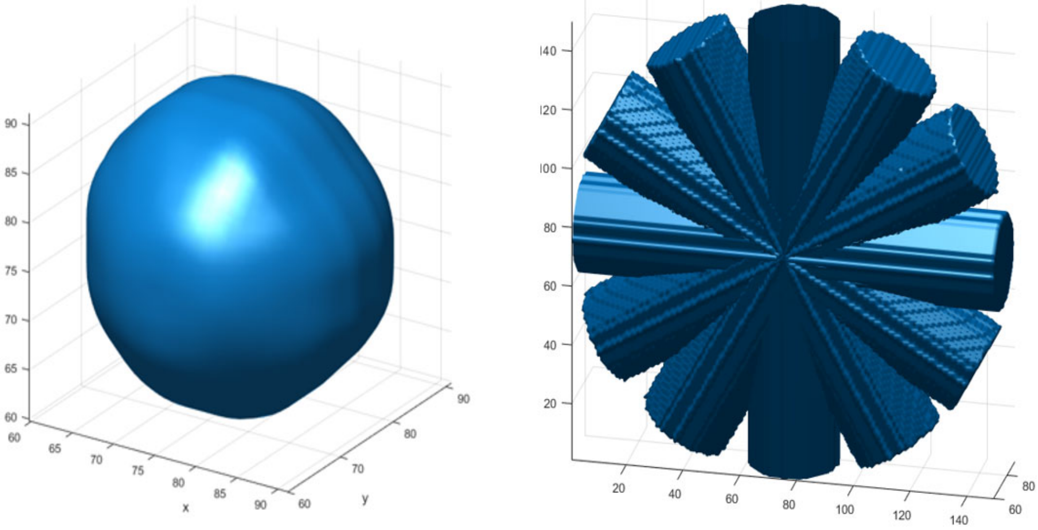

a) b)

Fig. 3.5. 3D Reconstruction and Multiplication of Projections from Different Angles for our Sample.

3.3. Results and Discussion

3.3.1. Detection Evaluation

To evaluate the performance of our proposed method for detecting and segmenting amoebas in liquids using holotomography, we measured the accuracy of the method in terms of its ability to correctly identify the position of the amoeba based on the value of the c parameter returned by our setup (Table 3.1). To compare the performance of our method with other state-of-the-art methods, we also calculated the percentage of accuracy for the Potential Field Segmentation (PFS), Edge Detection, Template Matching, and Clustering methods in detecting the centers of the amoebas. The results of these comparisons provide insight into the relative effectiveness of these different approaches for detecting and segmenting amoebas in liquids. Potential Field Segmentation (PFS) is a method used in image processing and computer vision to segment an image into different regions or objects [23]. It works by creating a potential field for each pixel in the image, with the strength of the field determined by the pixel's intensity or color. Pixels with similar intensities are attracted to each other, causing them to cluster together and form a segment. Edge detection is a method used to identify the boundaries of objects in an image. It works by detecting sudden changes in pixel intensity or color, which typically occur at the edges of objects. There are many different edge detection algorithms, each with its own strengths and weaknesses [20]. Template matching is a method used to find a template or pattern in an image [24]. It works by sliding the template over the image and comparing the template to each subregion of the image. If the template and subregion match, the method records the location of the match. Template matching can be used for object recognition, image registration, and many other applications. Clustering is a method used to group data points into clusters based on their similarity. It is often used in image processing and computer vision to segment an image into different regions or objects. In image segmentation, the principle of clustering algorithms involves partitioning an image into meaningful regions or objects based on similarities in pixel values, colors, textures, or other visual features. Clustering algorithms such as K-Means, DBSCAN, or hierarchical clustering can be applied to group pixels with similar characteristics into distinct clusters, effectively segmenting the image into semantically meaningful regions. This process aids in tasks like object detection, image recognition, and computer vision by isolating and identifying objects or regions of interest within the image [21, 22].

Table 3.1. Proposed method percentage in returning the parameter c inside the amoeba and the average time compared the state of art.

Methods	**Accuracy (%)**			**Time average (seconds)**
	Inside Amoeba	**Edge Amoeba**	**Outside Amoeba**	
Edge detection method [20]	80 %	19 %	1 %	9.1007
Template matching method [24]	90,5 %	5,5 %	4 %	7.4689
Clustering method [21, 22]	96 %	2 %	2 %	13.1247
Potential field method [23]	95 %	0	5 %	38.1643
Proposed method	98 %	2 %	0 %	1.4322

3.3.2. Segmentation Evaluation

Image segmentation techniques such as the Geodesic Active Contour (GAC) [25], Localized Active Contour (LAC) [24], and Active Contour driven by Cuckoo Search (ACCS) [28] have been widely used for their ability to extract objects of interest from images. GAC is a fast method that can handle topological changes well but may struggle with noisy or concave objects. On the other hand, LAC is more sensitive to local features and less sensitive to global features than GAC but may be more prone to getting stuck in local minima [27]. ACCS combines the principles of active contours with the Cuckoo Search optimization algorithm, allowing it to more effectively escape local minima and find the global minimum energy solution. However, ACCS may be slower due to the added computational cost of the Cuckoo Search algorithm. Each of these methods has its own strengths and limitations, and the appropriate method to use may depend on the specific needs of the application.

In comparison (Table 3.2) to the Geodesic Active Contour (GAC) method, our method showed improved sensitivity and specificity, as well as a lower average time for image processing. The Dice coefficient was similar between the two methods, but our method had a slightly smaller Hausdorff distance. The Localized Active Contour (LAC) method had similar sensitivity and specificity to our method, but a lower Dice coefficient and a larger Hausdorff distance. The Active Contour driven by Cuckoo Search (ACCS) method had the highest sensitivity and Dice coefficient, but the longest average processing time and the largest Hausdorff distance. Overall, our method strikes a good balance between accuracy and efficiency, making it a strong contender in image segmentation tasks.

Table 3.2. Sensitivity, Dice, Hausdorff distance, Specificity, and elapsed time rates obtained from the optimal contour of the images of our sample reached by using the Geodesic Active Contour (GAC), the Localized Active Contour (LAC), the Active Contour driven by Cuckoo Search (ACCS), and the proposed method (Proposed).

Patients	**Method**	**Sen**	**D (AVG± ±SD×10^{-4})**	**H_d**	**Spe**	**Times (s)**
Captured image at 0°	GAC	0.7083 ±1.1	0.7539 ±6.2	3.2311 ±2.5	0.9645±0.6	12.8450 ±1.2
	LAC	0.8905 ±2.5	0.9371 ±3.2	2.6478 ±2.6	0.9772±2.1	11.2406 ±1.9
	ACCS	0.9391 ±7.4	0.9384 ±9.0	2.7448 ±5.2	0.9240±1.2	18.1200 ±2.0
	Proposed	0.9798 ±0.6	0.9876 ±0.1	2.7902±0.1	0.9969±1.5	1.4321 ±0.1
Captured image at 30°	GAC	0.6854 ±0.0	0.7978 ±4.3	4.3569 ±6.1	0.9913 ±4.5	12.8352 ±1.0
	LAC	0.8152 ±5.4	0.9241 ±2.2	4.5010 ±2.0	0.9907 ±2.8	11.2316 ±1.1
	ACCS	0.9243 ±1.5	0.9685 ±0.8	3.6050 ±2.5	0.9969 ±1.1	18.1340 ±2.6
	Proposed	0.9849 ±0.3	0.9792 ±0.6	2.1597 ±0.2	0.9987 ±0.1	1.4401 ±0.3
Captured image at 60°	GAC	0.6804 ±5.3	0.8689 ±5.2	6.5823 ±2.5	0.9702 ±0.3	12.7052 ±1.4
	LAC	0.6915 ±1.3	0.7917 ±4.2	5.7490 ±3.5	0.8914 ±0.1	10.1016 ±2.1
	ACCS	0.9574 ±2.8	0.9620 ±4.1	3.8760 ±5.1	0.9892 ±0.7	18.1340 ±3.1
	Proposed	0.9978 ±0.1	0.9898 ±0.0	2.0194 ±1.1	0.9987 ±0.0	1.4301 ±0.5
Captured image at 90°	GAC	0.5435 ±3.6	0.6842 ±0.2	4.5432 ±7.7	0.9976 ±1.7	12.9528 ±8.7
	LAC	0.6951 ±2.2	0.7845 ±1.3	4.0214 ±3.7	0.9850 ±4.6	9.8972 ±8.0
	ACCS	0.8785 ±3.5	0.9456 ±1.4	3.0145 ±2.3	0.9679 ±7.4	17.8972 ±5.4
	Proposed	0.9876 ±0.1	0.9934 ±0.5	2.0124 ±1.1	0.9899 ±0.2	1.4401 ±1.0
Captured image at 120°	GAC	0.8267 ±3.4	0.7382 ±2.8	4.8558 ±3.9	0.9804 ±3.5	12.5467 ±8.6
	LAC	0.8678 ±2.0	0.8243 ±0.0	6.5701 ±1.2	0.9906 ±0.5	10.1245 ±2.8
	ACCS	0.9242 ±2.1	0.9780 ±0.2	3.6437 ±1.1	0.9881 ±4.6	18.7682 ±1.8
	Proposed	0.9896 ±0.1	0.9964 ±0.2	2.3559 ±1.1	0.9967 ±0.3	1.4330 ±0.6
Captured image at 150°	GAC	0.7952 ±5.4	0.8256 ±2.7	3.2310 ±2.0	0.9920 ±2.2	12.3899 ±7.4
	LAC	0.8645 ±0.3	0.7981 ±0.7	3.2453 ±0.0	0.9965 ±7.9	10.5313 ±0.9
	ACCS	0.9145 ±2.0	0.9680 ±3.3	2.8947 ±6.7	0.9988 ±2.3	17.3692 ±5.0
	Proposed	0.9956 ±0.8	0.9962 ±2.2	2.0420 ±0.1	0.9998 ±1.7	1.4310 ±4.6

The evolution of the initial contour detected by our system is performed using the proposed active contour model, which is programmed using finite differences after the energy function has been discretized and linearized. This allows us to track the evolution of the contour as it moves towards the optimal solution for the given energy function Eq. (3.3). The finite difference approach enables us to approximate the derivatives of the energy function in a computationally efficient manner, and the linearization allows us to solve for the update to the contour at each iteration using a set of linear equations. By iteratively updating the contour according to the optimized solution, we are able to accurately extract the object of interest from the image.

$$E_{i,j} = \alpha C_{i,j} + \beta |I - m_{i,j}|^2 + \gamma |I - M_{i,j}|^2, \qquad (3.3)$$

where $\alpha = \beta = \gamma = 1$ are fixed parameters. $C_{i,j}$ is the initial contour detected by the proposed method. $m_{i,j}$ is the average of the input RM image I(x,y) inside the initial contour $C_{i,j}$. $M_{i,j}$ is the average of the input RM image I(x,y) outside the initial contour $C_{i,j}$ and

$$0 \le Sen = \frac{TP}{TP+FN} \le 1,\ 0 \le D = \frac{TP}{TP+\frac{FP+FN}{2}} \le 1,$$

$$0 \le Sep = \frac{TN}{TN+FP} \le 1,\ H_d(G,S) = \max\left\{\max_{a\in G}\min_{b\in S}\|a-b\|, \max_{b\in S}\min_{a\in G}\|b-a\|\right\}$$

3.4. Conclusion

In summary, our use of holographic tomography to extract and segment amoebas from water samples has allowed us to visualize the three-dimensional structure and movement of these organisms in detail, study their behavior and interactions with their environment. The use of multiple CCD cameras to record holograms at different angles has improved the resolution and contrast of the images, resulting in clearer and more detailed visualization of the amoebas. The extraction of the maximum value from the in-phase component of the scanned data allows for the reliable and precise localization of amoeba positions. Concurrently, the application of active contour theory enables the meticulous delineation and segmentation of amoebas from their surrounding environment. This synergistic approach ensures a scientifically rigorous methodology for amoeba detection and analysis. Simultaneously, 3D reconstruction of amoebas provides critical insights into their structure and behavior, enhancing our understanding of their ecological roles and potential impacts on human health. Overall, our results demonstrate the effectiveness of holographic tomography as a powerful tool for studying the internal structure and properties of biological samples and have important implications for understanding the behavior and interactions of amoebas in aquatic environments. This knowledge is instrumental in assessing water quality and safety for human consumption, contributing to essential public health considerations.

Acknowledgment

We would like to express our gratitude to the organizers of the Brain Tumor Segmentation (BraTS) challenge for providing us with the BRATS 2012 and 2013 databases. These datasets are instrumental in our research and contribute significantly to our work in the field of medical image analysis. Thank you for your valuable support [29].

References

[1]. C. Depeursinge, P. Marquet, L. Magaud, Digital holographic microscopy: a review, *Advances in Optics and Photonics*, Vol. 2, Issue 2, 2010, pp. 238-278.

[2]. D. Kim, Y. Kim, D. Kim, Digital holographic microscopy, *Optics Letters*, Vol. 30, Issue 22, 2005, pp. 3033-3035.

[3]. P. Gu, H. Chen, L. Zeng, Digital holographic microscopy for three-dimensional imaging and analysis of biological cells, *Chinese Physics Letters*, Vol. 28, Issue 4, 2011, 044202.

[4]. J. Xu, W. Chen, J. Li, X. Wang, Detection and identification of free-living amoebae in water environments: A review, *Environmental Science and Pollution Research*, Vol. 27, Issue 24, 2020, pp. 29791-29801.

[5]. R. Bhojwani, D. Bhojwani, V. Khanna, Amoebiasis: An overview, *Journal of Global Infectious Diseases*, Vol. 11, Issue 1, 2019, pp. 1-7.

[6]. L. Zeng, C. Ma, Optical tomography for imaging and sensing, *Laser Photonics Reviews*, Vol. 7, Issue 1, 2013, pp. 94-119.

[7]. Bazow B., Lam V.K., Phan T., Chung B.M., Nehmetallah G., Raub C.B., Digital Holographic Microscopy to Assess Cell Behavior, Methods in Molecular Biology, 2644, 2023, pp. 247–266.

[8]. Gu, J. Pan, L. Chen, Digital holographic microscopy: a review, Journal of Biomedical Optics, Vol. 16, Issue 11, 2011, 111401.

[9]. Wang K., Song L., Wang C., et al., On the use of deep learning for phase recovery, Light: Science & Applications, 13, 2024, 4.

[10]. Zhang, H. Chen, Digital holographic microscopy for cells and tissues, Journal of Biomedical Optics, Vol. 19, Issue 8, 2014, 086008.

[11]. Y. Kim, J. Kim, S. Kim, Three-dimensional imaging of transparent objects by digital holographic microscopy, *Optics Letters*, Vol. 30, Issue 24, 2005, pp. 3382-3384.

[12]. E, Ouabida, A. Essadique, A. Bouzid, Vander Lugt Correlator based active contours for iris segmentation and tracking, *Expert Systems with Applications*, Vol. 71, 2017, pp. 383-395.

[13]. A. Essadike, E. Ouabida, A. Bouzid, Brain tumor segmentation with Vander Lugt Correlator based active contour, *Computer Methods and Programs in Biomedicine*, Vol. 160, 2018, pp. 103-117.

[14]. A. Essadike, E. Ouabida, A. Bouzid, Optical scanning holography for tumor extraction from brain magnetic resonance images, *Optics Laser Technology*, Vol. 127, 2020, 106158.

[15]. E. Ouabida, A. Essadike, A. Bouzid, Optical correlator based algorithm for driver drowsiness detection, *Optik*, Vol. 204, 2020, 164102.

[16]. E. Ouabida, A. Essadike, A. Bouzid, Automated segmentation of ophthalmological images by an optical based approach for early detection of eye tumor growing, *Physica Medica*, Vol. 48, 2018, pp. 37-46.

[17]. El-Ouarzadi A., Cherkaoui A., Essadike A., Achaoui Y., Bouzid A., Brain Tumor Detection and Segmentation Using a Hybrid Optical Method by Active Contour, in Proceedings of the 2023 International Conference on Digital Age & Technological Advances (DATA), Morocco, 2023, pp. 132–137.

[18]. A. Cherkaoui, A. El-Ouarzadi, A. Essadike, A. Bouzid, Automatic brain tumor detection and segmentation using enhanced optical scanning holography and active contour model in MRI, *Sensors & Transducers*, Vol. 262, Issue 2, 2023, pp. 13-22.

[19]. J. Canny, A computational approach to edge detection, *IEEE Transactions on Pattern Analysis and Machine Intelligenc*e, Vol. 8, Issue 6, 1986, pp. 679-698.

[20]. A. K. Jain, Data clustering: 50 years beyond K-means, *Pattern Recognition Letters*, Vol. 31, Issue 8, 2010, pp. 651-666.

[21]. Xu R., Wunsch D., Survey of clustering algorithms, IEEE Transactions on Neural Networks, 16, 3, 2005, pp. 645–678.

[22]. J. A. Lee, Image segmentation by potential field computation, *Computer Vision and Image Understanding*, Vol. 55, Issue 1, 1991, pp. 7-27.

[23]. L. Zhang, A survey of thresholding techniques, *Computer Vision and Image Understanding*, Vol. 104, Issue 1, 2004, pp. 59-78.

[24]. V. Caselles, R. Kimmel G. Sapiro, Geodesic active contours, *International Journal of Computer Vision*, Vol. 22, 1997, pp. 61-79.

[25]. I. Cabria, I. Gondra, MRI segmentation fusion for brain tumor detection, *Information Fusion*, Vol. 36, 2017, pp. 1-9.

[26]. E. Ilunga-Mbuyamba, J. G. Avina-Cervantes, A. Garcia-Perez, et al., Localized active contour model with background intensity compensation applied on automatic MR brain tumor segmentation, *Neurocomputing*, Vol. 220, 2017, pp. 84-97.

[27]. U. Baid, et al., The RSNA-ASNR-MICCAI BraTS 2021 Benchmark on Brain Tumor Segmentation and Radiogenomic Classification, *arXiv preprint*, 2021, arXiv:2107.02314.

[28]. B. H. Menze, A. Jakab, S. Bauer, J. Kalpathy-Cramer, K. Farahani, J. Kirby, et al., The multimodal brain tumor image segmentation benchmark (BRATS), *IEEE Transactions on Medical Imaging*, Vol. 34, Issue 10, 2015, pp. 1993-2024.

[29]. S. Bakas, H. Akbari, A. Sotiras, M. Bilello, M. Rozycki, J. S. Kirby, et al., Advancing the cancer genome atlas glioma MRI collections with expert segmentation labels and radiomic features, *Nature Scientific Data*, Vol. 4, 2017, 170117.

Advances in Signal Processing
Volume 3

Sergey Y. Yurish, Editor

This volume continues the series' mission to showcase high-quality contributions that reflect both the theoretical foundations and the rapidly expanding application landscape of modern signal processing. Across its chapters, the reader will find a balanced blend of wearable sensing and biomedical signal acquisition, mathematical and algorithmic methods with relevance to data and signal models, and computational imaging for detection and segmentation tasks - three directions that increasingly converge in today's interdisciplinary research and development.

This book should prove useful to a broad audience: graduate students seeking well-motivated examples and methods; academic researchers exploring cross-disciplinary directions; and engineers developing practical systems in healthcare, sensing, imaging, and analytics. We hope that the ideas collected here will not only inform current work but also inspire new collaborations across the diverse communities that contribute to - and benefit from - advances in signal processing.

IFSA

ISBN 978-84-09-69173-9

9 788409 691739